Reactivity and leaching potential of municipal solid waste incineration (MSWI) bottom ash as supplementary cementitious material and precursor for alkali-activated materials

Chen, Boyu; Zuo, Yibing; Zhang, Shizhe; de Lima Junior, Luiz Miranda; Liang, Xuhui; Chen, Yun; van Zijl, Marc Brito; Ye, Guang

DOI
10.1016/j.conbuildmat.2023.133890

Publication date
2023

Document Version
Final published version

Published in
Construction and Building Materials

Citation (APA)
Chen, B., Zuo, Y., Zhang, S., de Lima Junior, L. M., Liang, X., Chen, Y., van Zijl, M. B., & Ye, G. (2023). Reactivity and leaching potential of municipal solid waste incineration (MSWI) bottom ash as supplementary cementitious material and precursor for alkali-activated materials. *Construction and Building Materials*, *409*, Article 133890. https://doi.org/10.1016/j.conbuildmat.2023.133890

Construction and Building Materials 409 (2023) 133890

Contents lists available at ScienceDirect

Construction and Building Materials

journal homepage: www.elsevier.com/locate/conbuildmat

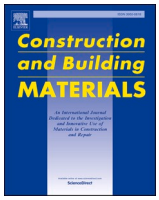

Reactivity and leaching potential of municipal solid waste incineration (MSWI) bottom ash as supplementary cementitious material and precursor for alkali-activated materials

Boyu Chen [a,*], Yibing Zuo [b], Shizhe Zhang [a,c], Luiz Miranda de Lima Junior [a], Xuhui Liang [a], Yun Chen [a], Marc Brito van Zijl [c], Guang Ye [a,d]

[a] Department of Materials and Environment (Microlab), Faculty of Civil Engineering and Geoscience, Delft University of Technology, Delft, The Netherlands
[b] School of Civil and Hydraulic Engineering, Huazhong University of Science and Technology, Wuhan 430074, China
[c] Mineralz (part of Renewi), Van Hilststraat 7, 5145 RK Waalwijk, The Netherlands
[d] Magnel-Vandepitte Laboratory, Department of Structural Engineering and Building Materials, Ghent University, 9052 Ghent, Belgium

ARTICLE INFO

Keywords:
MSWI bottom ash
Supplementary cementitious material
Alkali-activated materials
Reactivity
Leaching

ABSTRACT

This work evaluated the reactivity and leaching potential of municipal solid waste incineration (MSWI) bottom ash as supplementary cementitious material (SCM) and precursor for alkali-activated materials (AAM). The chemical composition of the amorphous phase in MSWI bottom ash was found to be in the same range as that of Class F coal fly ash. The reactivity of MSWI bottom ash as SCM and AAM precursor was tested to be much lower than that of blast furnace slag, but similar to that of Class F coal fly ash. The method of thermodynamic modeling was found useful in providing references for the mix design of MSWI bottom ash-based AAM. Grinding MSWI bottom ash into powder for the application of SCM and AAM precursor increased its leaching potential. Based on the findings of this study, recommendations were provided on how to use MSWI bottom ash to prepare blended cement pastes and AAM.

1. Introduction

With continued population and economic growth, global municipal solid waste generation is expected to reach 3.40 billion tonnes by 2050, almost twice as much as that in 2016 [1]. Over the past few decades, the municipal solid waste sent to waste-to-energy plants around the world has increased rapidly, especially in countries like China and India [2–5]. The disposal of municipal solid waste incineration (MSWI) residue is becoming the primary environmental concern for the wide application of waste incineration techniques [6]. Although municipal solid waste incineration significantly reduces the amount of waste sent to landfills, the mass of waste incineration residue can still reach around 20 % of the waste input [7–9]. The ash collected at the bottom of the incinerator is the main residue generated after municipal solid waste incineration, accounting for around 80 % to 90 % of the total incineration residue [10,11]. In recent years, the utilization of MSWI bottom ash as a mineral resource for construction materials has attracted increasing attention.

Cement production is estimated to contribute about 8 % of anthropogenic global CO_2 emissions [12]. Reducing the proportion of clinker in cement can help reduce the carbon footprints of construction materials [13]. The life cycle analysis results indicated that replacing Portland cement with alkali-activated materials could reduce 40 to 80 % of CO_2 emissions [14–22]. The alkali-activated materials (AAM) are clinker-free binders prepared by reacting aluminosilicate precursors with alkaline solutions [23]. At present, blast furnace slag and coal fly ash are the most commonly used supplementary cementitious materials and AAM precursors. However, according to the World Business Council for Sustainable Development, the availability of blast furnace slag and coal fly ash will decrease in the next 30 years [24]. There is a need to explore alternative industrial by-products for the low-carbon transition of the cement industry [25].

The application of MSWI bottom ash as supplementary cementitious material (SCM) and AAM precursor strongly depends on its reactivity. In MSWI bottom ash, the amorphous phase, which mainly consists of waste glass particles, is found to be the primary reactive phase [26,27]. Although the content of the amorphous phase was quantified in previous work, the chemical composition of the amorphous phase was not determined [28]. Up till now, the contribution of the amorphous phase

* Corresponding author.
E-mail address: B.Chen-4@tudelft.nl (B. Chen).

https://doi.org/10.1016/j.conbuildmat.2023.133890
Received 9 February 2023; Received in revised form 9 September 2023; Accepted 18 October 2023
Available online 24 October 2023

to the reactivity of MSWI bottom ash has not been very well understood.

Different standardized methods have been used to measure the pozzolanic reactivity of MSWI bottom ash [28]. However, there is no standardized method for measuring the reactivity of MSWI bottom ash as AAM precursor. The alkali activation in AAM is generally considered as a series of reactions involving dissolutions of precursors and precipitation of products [29,30]. The dissolution of precursors in alkaline solution is the first step in the chemical reaction to form AAM [29,30]. Previous researchers assessed the reactivity of MSWI bottom ash as AAM precursor by measuring the amount of SiO_2 and Al_2O_3 that can dissolve from MSWI bottom ash in alkaline solutions [31,32]. However, this method neglects the contribution of other elements to the reaction product formation and thus provides limited information about the reactivity of MSWI bottom ash.

Thermodynamic modeling combined with accurate and complete thermodynamic databases can predict the phase formation in alkali-activated materials [33]. This method has been used to simulate the phase diagrams for alkali-activated blast furnace slag, when NaOH, Na_2SiO_3, $Na_2Si_2O_5$, Na_2CO_3, or Na_2SO_4 is used as activator [34]. The phase assemblages and pore solution predicted by thermodynamic modeling can be used to guide the mix design of alkali-activated materials [35]. It is meaningful to explore the possibility of using thermodynamic modeling to simulate the phase assemblages and pore solution in alkali-activated MSWI bottom ash. The simulation results may provide insight into the reactivity of MSWI bottom ash as AAM precursor and can be used as references for the mix design of alkali-activated MSWI bottom ash.

Soluble salts and heavy metals present in MSWI bottom ash may leach into the environments during the use stage of MSWI bottom ash-containing construction materials. When used as SCM or AAM precursor, MSWI bottom ash is usually ground into powder through mechanical treatments. The size reduction of MSWI bottom ash can facilitate the leaching of heavy metals. Giro-Paloma et al. [36] ground MSWI bottom ash aggregates (0–2 mm) into fine powder for the application of AAM precursor. The concentrations of As, Cr, Mo, and Sb in the leachate of MSWI bottom ash powder almost doubled that in the leachate of MSWI bottom ash aggregates. The leaching of contaminants from MSWI bottom ash determines its acceptable dosage in blended cement and AAM. Therefore, measuring the leaching potential of MSWI bottom ash powder is required prior to its application as SCM and AAM precursor.

This work aims to provide a comprehensive understanding of the reactivity and leaching potential of MSWI bottom ash as SCM and AAM precursor and provide guidance to the mix design of blended cement pastes and AAM prepared with MSWI bottom ash. The following aspects are covered in this work.

- The chemical composition of the amorphous phase in MSWI bottom ash is determined and compared with that of the amorphous phase in blast furnace slag and Class F coal fly ash.
- The reactivity of MSWI bottom ash as SCM and AAM precursor is measured and compared with that of blast furnace slag and Class F coal fly ash. A dissolution test is proposed to measure the reactivity of MSWI bottom ash as AAM precursor.
- The solid phase assemblages and pore solution compositions of alkali-activated MSWI bottom ash paste are predicted with thermodynamic modeling. The modeling results are compared with experimental data reported in the literature to assess the reliability of the simulation. The modeling results provide references for the mix design of MSWI bottom ash-based AAM.
- The leaching of contaminants from MSWI bottom ash is assessed, and the risks of environment contamination caused by the addition of MSWI bottom ash in blended cement pastes and alkali-activated pastes are also discussed.

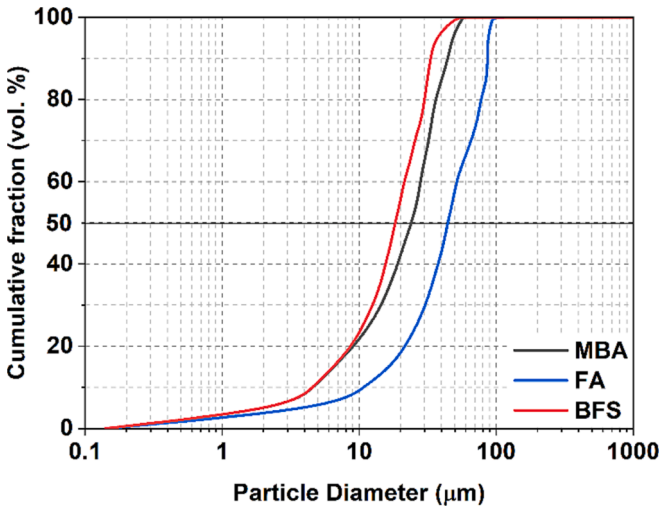

Fig. 1. Particle size distribution of MBA, BFS, and FA determined by laser diffraction method.

2. Materials and methods

2.1. Materials

The MSWI bottom ash powder used in this work was obtained after the mechanical treatments of MSWI bottom ash aggregates (4–11 mm). The production of MSWI bottom ash aggregates followed the same method as Keulen et al. [37], where MSWI bottom ash was treated with dry separation, wet separation, and weathering. The mechanical treatments consist of crushing, grinding, and sieving. In this context, the MSWI bottom ash powder is named mechanically treated MSWI bottom ash (MBA). The particle size of MBA is below 63 μm. MBA also contains around 0.13 wt% residual metallic Al.

The Class F coal fly ash (FA) and blast furnace slag (BFS) were used as reference materials. BFS met the specifications of NEN-EN 15167–1 [38] and was provided by Eco_2cem Benelux B.V.. FA complied with the requirements of Class F coal fly ash and was supplied by Vliegasunie B.V.. The densities of MBA, FA, and BFS, as measured by pycnometer, are 3.2 g/cm^3, 2.7 g/cm^3, and 3.5 g/cm^3, respectively. The particle size distribution of these materials was measured using the laser diffraction method (Malvern Mastersizer). As illustrated in Fig. 1, FA with D_{50} of 44.2 μm is coarser than MBA and BFS. The D_{50} of MBA is 24 μm, larger than that of BFS (18.3 μm). The free lime content in MBA is zero, as measured by following the NEN-EN1744-1 [39].

2.2. Characterization techniques

2.2.1. Chemical and mineralogical compositions

The Panalytical Axio Max WD-XRF spectrometer was used to measure the chemical composition of MBA, FA, and BFS. The unburned organic content in the raw materials, also referred to as loss on ignition (LOI), was measured according to NEN-EN 1744–7 (2010) at 550 ℃.

The mineralogical compositions of MBA, FA, and BFS were determined by X-ray diffraction (XRD) techniques using Bruker D8 Advance diffractometer. For the sample preparation, the raw materials were manually milled in agate mortar to ensure their particle sizes were between 1 and 5 μm. The mineral phases were identified with Bruker software DiffracSuite.EVA 4.3.

For the quantitative XRD analysis (QXRD), ten percent (10 wt%) of silicon powder was mixed with MSWI bottom ash powder during the sample preparation process. The amount of each mineral phase was estimated by using the Rietveld method with the software Profex-BGMN [40]. The crystal structure models taken from the Inorganic Crystal Structure Database (ICSD) were used to fit the observed XRD pattern.

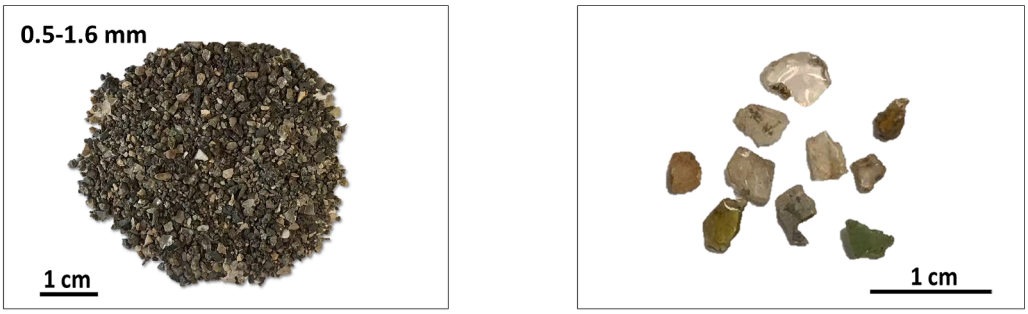

(a) 0.5- 1.6 mm size fraction of MSWI bottom ash aggregates (b) Manually separated glass particles

Fig. 2. (a) Image of 0.5–1.6 mm size fraction of MSWI bottom ash aggregates. (b) Image of glass particles separated from 0.5 to 1.6 mm size fraction.

2.2.2. Analysis of amorphous phase

The content of the amorphous phase in MBA was determined by quantitative XRD analysis (QXRD) analysis, the same method as that used in our previous work [41]. The percentages of SiO_2, Al_2O_3, CaO, Fe_2O_3, Na_2O, K_2O, and MgO present in the amorphous phase of MBA were obtained by subtracting the percentages of these oxides in crystalline phases from the bulk composition of MBA [40]. The proportions of SiO_2, Al_2O_3, CaO, Fe_2O_3, Na_2O, K_2O, and MgO in the crystalline phases were calculated from the Rietveld refinement results with the software Profex-BGMN [40]. The bulk compositions refer to the chemical compositions determined by the XRF measurement. The methods used in the analysis of the amorphous phase MBA were also used to study the amorphous phase of FA and BFS.

The existence of the amorphous phase was further proved by performing chemical dissolution treatments on MBA. This method was also used by Ma [42] and Zhang et al. [43] to determine the contents of the amorphous phase and the reactive silica in Class F coal fly ash. According to NEN-EN 196-2 [44], the fraction of the SiO_2 dissolved during the chemical dissolution treatments is defined as reactive silica content. The treatments were performed following the description in NEN-EN 196-2 [44]. MBA was successively treated with a hydrochloric acid solution and boiling potassium hydroxide solution. The insoluble residue of MBA was ignited at 950 °C. After all these steps, the amorphous phase, such as the glass and the organics, was removed from MBA. The insoluble residue was analyzed with XRD and XRF. The test results were compared with that of MBA to evaluate the composition changes.

Since waste glass is one of the primary sources of the amorphous phase in MBA, the chemical composition of the glass particles in MBA was compared with that of the amorphous phase of MBA. The glass particles in MBA were analyzed by measuring the chemical and mineralogical compositions of the waste glass particles initially present in MSWI bottom ash aggregates (4–11 mm). The glass particles were manually separated from the 0.5–1.6 mm size fraction of MSWI bottom ash aggregates according to their transparent appearance. The images of the MSWI bottom ash particles within the 0.5–1.6 mm size fraction and the separated glass particles are illustrated in Fig. 2. After grinding separated glass particles into fine powders, the compositions of glass particles were determined by XRF and XRD analysis, in the same way as that for MBA.

It is worth mentioning that there are two reasons for choosing 0.5–1.6 mm size fraction for glass composition analysis. First, the mineralogical composition of MBA is also the same as that of MSWI bottom ash aggregates. The chemical and mineralogical composition varies slightly among different size fractions of MSWI bottom ash aggregates [45]. Second, the 0.5–1.6 mm size fraction accounts for around 50 wt% of MSWI bottom ash aggregates. Separating glass particles from 0.5 to 1.6 mm size fraction is much easier than the fraction with smaller particles.

2.2.3. Reactivity test for the application as SCMs

The pozzolanic reactivity of MBA, which determines its application as SCM, was measured using isothermal calorimetry test. The experiment design followed the R^3 method [46,47], where the reaction of SCM in blended cement pastes is mimicked. The test was conducted by following the procedures and protocols described in ASTM C1897-20 [47]. The test pastes (also called R^3 pastes) were prepared by mixing 11.11 g SCM with 33.33 g $Ca(OH)_2$, 5.56 g $CaCO_3$, 0.24 g KOH, 1.2 g K_2SO_4, and 60 g deionized water [46]. The supplementary cementitious materials (SCMs) measured in this work are MBA, BFS, and FA. The heat released during the hydration of the pastes at 40 °C until 7 days was recorded by isothermal conduction calorimeter (TAM-Air-314). The cumulative heat released by the pozzolanic reaction of 1 g of SCM was calculated after recording the heat release for 7 days. It is worth noting that the compressive strength was not used as an indicator for the pozzolanic reactivity of MBA. Since MBA contains metallic Al, the method of strength measurement will underestimate the pozzolanic reactivity of MBA. The metallic Al in MBA will react with $Ca(OH)_2$ and release hydrogen gas, causing a strength decrease [48].

2.2.4. Reactivity test for the application as AAM precursors

The solubility of precursor in alkaline solution determines the amount of Si, Al, Ca, Fe, and Mg that can participate in the formation of reaction products. The reactivity of MBA as AAM precursor was assessed by dissolution test, where the reaction of MBA in the alkaline environment of AAM was reproduced. The same test was performed on BFS and FA to compare with the test results of MBA.

The reactivity test was designed by adapting the dissolution test proposed for measuring the reactivity of synthesized blast furnace slag and coal fly ash in alkaline environment [49]. The solid-to-liquid ratio was set as 1 g to 1 L. At this ratio, the solution was in the undersaturated condition, preventing the precipitation of the reaction products to the largest possible extent [49,50]. To accelerate the dissolution of tested precursors, the pH of the NaOH solution used in the tests was slightly higher than that of the pore solution of alkali-activated slag (13.77–14.67) and alkali-activated fly ash (13.08–14.07) reported by Zuo et al. [51]. The sodium hydroxide solution with different molarity (4 M, 5 M, and 6 M) was selected to mimic the alkaline environment in the pore solution of AAM. The pH of 4 M, 5 M, and 6 M NaOH solutions is 14.6, 14.7, and 14.8, respectively.

In the experiment, 1 g of precursor (MBA, FA, or BFS) was dissolved in 1 L NaOH solution stored in a polypropylene container, and the solution was stirred continuously for 24 h. The whole setup was kept in a temperature-controlled room at 25 °C. After the dissolution test, the concentrations of dissolved Si, Al, Ca, Fe, and Mg in the solution were determined. The filtered solutions were diluted with nitric acid (0.2 vol %). The diluted solutions were analyzed through inductively coupled plasma-optical emission spectroscopy (ICP-OES), model PerkinElmer Optima 5300DV.

Table 1
End-members in the CNASH_ss model used to describe the C-(N-)A-S-H gel [54].

End-member groups	End-member names	Formulae	Molar ratios		
			Ca/Si	Al/Si	Na/Si
C-A-S-H	5CA	$(CaO)_{1.25}\cdot(Al_2O_3)_{0.125}\cdot(SiO_2)\cdot(H_2O)_{1.625}$	1.25	0.25	0
	INFCA	$(CaO)\cdot(Al_2O_3)_{0.15625}\cdot(SiO_2)_{1.1875}\cdot(H_2O)_{1.65625}$	0.84	0.26	0
C-N-A-S-H	5CNA	$(CaO)_{1.25}\cdot(Na_2O)_{0.25}\cdot(Al_2O_3)_{0.125}.(SiO_2)\cdot(H_2O)_{1.25}$	1.25	0.25	0.50
	INFCNA	$(CaO)\cdot(Na_2O)_{0.34375}\cdot(Al_2O_3)_{0.15625}\cdot(SiO_2)_{1.1875}\cdot(H_2O)_{1.3}$	0.84	0.26	0.58
C-N-S-H	INFCN	$(CaO)\cdot(Na_2O)_{0.3125}\cdot(SiO_2)_{1.5}\cdot(H_2O)_{1.1875}$	0.67	0	0.42
C-S-H	T2C	$(CaO)_{1.5}\cdot(SiO_2)\cdot(H_2O)_{2.5}$	1.50	0	0
	T5C	$(CaO)_{1.25}\cdot(SiO_2)_{1.25}\cdot(H_2O)_{2.5}$	1.00	0	0
	TobH	$(CaO)\cdot(SiO_2)_{1.5}\cdot(H_2O)_{2.5}$	0.67	0	0

Table 2
End-members in the MA-OH-LDH_ss model used to describe the hydrotalcite-like phases [55].

End-member names	Formulae
M_4AH_{10}	$(MgO)_4\cdot(Al_2O_3)\ (H_2O)_{10}$
M_6AH_{12}	$(MgO)_6\cdot(Al_2O_3)\ (H_2O)_{12}$
M_8AH_{14}	$(MgO)_8\cdot(Al_2O_3)\ (H_2O)_{14}$

2.2.5. Thermodynamic modeling

Thermodynamic modeling was used to predict the solid phase assemblages and pore solution compositions of alkali-activated MBA paste, alkali-activated BFS paste, and alkali-activated FA paste. This information can be used to guide the application of MBA as AAM precursor. In the modeling, MBA was activated by NaOH solution. The reason for this mix design is to prevent the ions in the activator (especially Si^{4+}) from affecting the reaction of the ions released by MBA. The NaOH solution was reacted with 100 g MBA, 100 g BFS, or 100 g FA. The water-to-precursor ratio in these three AAM systems was kept at 0.35. The alkalinity of NaOH was represented as the percentage of Na_2O relative to the mass of the precursor.

The changes in phase assemblages were simulated by changing the Na_2O content in the activator from 2 wt% to 10 wt%. It was assumed that only the SiO_2, CaO, Al_2O_3, Fe_2O_3, Na_2O, K_2O, and MgO in the amorphous phase of MBA, FA, and BFS were reacted in alkali activation, and their reaction degree was 100 %. The remaining components in the amorphous phase, together with the crystalline phases, were considered as the un-reactive fraction. The AAM system was under (metastable) thermodynamic equilibrium conditions.

The thermodynamic calculations were performed using the Gibbs energy minimization software GEMS-Selektor v.3 (https://gems.web.psi.ch/) [52,53] and the Cemdata 18 database [33]. The ideal solid solution model (CNASH_ss) derived by Myers et al. [54] for calcium (sodium) aluminosilicate hydrate (C-(N-)A-S-H) gel was used to simulate the gel phases in alkali-activated blast furnace slag. The hydrotalcite-like phases formed in alkali-activated blast furnace slag were simulated with the solid solution model MA-OH-LDH_ss [55]. The ideal solid solution model (N(C)ASH_ss) proposed by Zuo [56] for sodium (calcium) aluminosilicate hydrate (N-(C-)A-S-H) gel was used for the simulation of gel phases formed in alkali-activated fly ash. The details of the end-members used in these three idea solid solution models are listed in Table 1, Table 2, and Table 3.

For the simulation of the gel phases formed in alkali-activated MBA paste, the selection of the ideal solid solution model was based on the types of reaction products detected in alkali-activated MSWI bottom ash by previous researchers. The reaction products of the alkali activation of MSWI bottom ash were mainly amorphous phases, including calcium silicate hydrate (C-S-H) gel [57–59], calcium aluminosilicate hydrate (C-A-S-H) gel [57], and sodium aluminosilicate hydrate (N-A-S-H) gel [60]. Therefore, apart from CNASH_ss model [54] and N(C)ASH_ss model [56], the CSHQ model [33,61] usually used for Portland cement simulation was also selected in the setting of the database. Table 4 provides the details of the end-members included in the CSHQ model.

2.2.6. Assessment of leaching potential

One stage batch test was used to assess the leaching of contaminants from MBA. The test was performed following the standard NEN-EN 12457–4 [62]. The leaching agent was mixed with MBA at the liquid-to-solid ratio of 10 L/kg. The mixture was agitated for 24 h. After the test, the eluate was filtered over a 0.45 μm membrane filter. The concentrations of heavy metals were measured by inductively coupled plasma-atomic emission spectroscopy (ICP-AES). The chloride (Cl), bromide (Br), and sulfate (SO_4^{2-}) in the filtered eluate were analyzed by ion chromatography (IC). The content of Fluoride (F) was determined by flow injection analysis with spectroscopic detection. The test results were compared with the limiting level described in the Dutch Soil Quality Decree, 2015 [63].

Table 4
End-members in the CSHQ model used to describe the C-S-H gel [33,61].

End-member names	Formulae	Molar ratios Ca/Si
TobH	$(CaO)_{2/3}\ (SiO_2)\ (H_2O)_{1.5}$	0.67
TobD	$(CaO)_{5/6}\ (SiO_2)_{2/3}\ (H_2O)_{1.83}$	1.25
JenH	$(CaO)_{1.33}\ (SiO_2)\ (H_2O)_{2.17}$	1.33
JenD	$(CaO)_{1.5}\ (SiO_2)_{0.67}\ (H_2O)_{2.5}$	2.24

Table 3
End-members in the N(C)ASHss model used to describe the N-(C-)A-S-H gel [56].

End-member groups	End-member names	Formulae	Molar ratios		
			Ca/Si	Al/Si	Na/Al
N-C-A-S-H	NCASH_1-0.1	$(Na_2O)_{0.05}\cdot(CaO)_{0.45}\cdot(Al_2O_3)_{0.5}\cdot(SiO_2)_1\cdot(H_2O)_1$	0.45	1.00	0.1
	NCASH_2-0.1	$(Na_2O)_{0.05}\cdot(CaO)_{0.45}\cdot(Al_2O_3)_{0.5}\cdot(SiO_2)_2\cdot(H_2O)_1$	0.23	0.50	0.1
	NCASH_3-0.1	$(Na_2O)_{0.05}\cdot(CaO)_{0.45}\cdot(Al_2O_3)_{0.5}\cdot(SiO_2)_3\cdot(H_2O)_1$	0.15	0.33	0.1
	NCASH_4-0.1	$(Na_2O)_{0.05}\cdot(CaO)_{0.45}\cdot(Al_2O_3)_{0.5}\cdot(SiO_2)_4\cdot(H_2O)_1$	0.11	0.25	0.1
N-A-S-H	NASH_1-1	$(Na_2O)_{0.5}\cdot(Al_2O_3)_{0.5}\cdot(SiO_2)_1\cdot(H_2O)_1$	0	1.00	1
	NASH_2-1	$(Na_2O)_{0.5}\cdot(Al_2O_3)_{0.5}\cdot(SiO2)_2\cdot(H_2O)_1$	0	0.50	1
	NASH_3-1	$(Na_2O)_{0.5}\cdot(Al_2O_3)_{0.5}\cdot(SiO_2)_3\cdot(H_2O)_1$	0	0.33	1
	NASH_4-1	$(Na_2O)_{0.5}\cdot(Al_2O_3)_{0.5}\cdot(SiO_2)_4\cdot(H_2O)_1$	0	0.25	1

Table 5
Chemical compositions of MBA, FA, and BFS, as determined by XRF analysis.

Compounds (wt.%)	MBA	FA	BFS
SiO_2	52.91	55.29	34.99
CaO	13.44	4.43	36.33
Al_2O_3	10.18	25.03	14.32
Fe_2O_3	9.29	6.94	0.40
Na_2O	4.24	0.91	0.24
K_2O	0.84	1.66	0.46
SO_3	0.70	0.73	1.36
Cl	0.27	0.01	0.02
P_2O_5	1.03	1.01	0.01
MgO	2.40	1.41	9.42
ZnO	0.55	0.03	–
CuO	0.31	0.01	0.18
TiO_2	1.12	1.23	1.21
MnO	0.21	0.04	0.26
PbO	0.09	0.01	–
Cr_2O_3	0.07	0.02	–
BaO	0.09	0.07	0.04
NiO	0.03	0.01	–
ZrO_2	–	0.06	0.04
SrO	0.04	0.12	0.05
SnO_2	0.02	–	–
Rb_2O	–	0.01	–
Nb_2O_5	–	–	–
Y_2O_3	–	0.01	0.01
V_2O_5	–	0.04	0.02
CeO_2	–	–	0.08
LOI_{550}	2.17	0.92	0.56
Sum	100	100	100

3. Results and discussion

3.1. Compositions of MBA

3.1.1. Chemical composition

The chemical composition of MBA provides information about the presence of major components and hazardous components (such as soluble salts and heavy metals). The chemical compositions of MBA, BFS, and FA are listed in Table 5. The chemical composition of MBA is within the same range as the compositional ranges reported for the MSWI bottom ash in existing literature [28]. In MBA, the main constituents are SiO_2, CaO, Al_2O_3, and Fe_2O_3. The SiO_2 content in MBA is 52.91 wt%, close to that in FA but higher than in BFS. The CaO content in MBA is 13.44 wt%, three times as much as that in FA but much lower than that detected in BFS. The amount of Al_2O_3 in MBA is 10.18 wt%, less than half of the Al_2O_3 content in FA. The Al_2O_3 content in MBA is around 4 wt% less than that in BFS. Regarding Fe_2O_3, its content in MBA is higher than in FA and BFS. In addition to the major components, the contents of heavy metals, unburned organics, equivalent alkalis (Na_2O_e), SO_3, and Cl are of concern when MBA is used as SCM or AAM precursor.

As illustrated in Table 5, MBA contains much more heavy metals, unburned organics, alkalis, and chloride than FA and BFS. Only the SO_3 content in MBA is lower than that in FA and BFS. Although the toxic heavy metal components, such as CuO, PbO, and Cr_2O_3, are present in trace amounts in MBA (<1 wt%), their contents are much higher in MBA than in FA and BFS. In MBA, the unburned organic content, referred to as LOI_{550}, is 2.17 wt%, more than two times as much as that in FA and BFS. The heavy metals and unburned organics in MSWI bottom ash were found to be the primary sources of the heavy metals leached from the building materials prepared with MSWI bottom ash [64].

The Na_2O_e content in MBA is 4.79 wt%, as calculated according to the equation $Na_2O_e = Na_2O + 0.658\ K_2O$. This value is 2.01 wt% and 0.54 wt% in FA and BFS, respectively. The Na_2O present in the waste glass is responsible for this high Na_2O_e content in MBA, which will be confirmed in section 3.1.3. For Portland cement concrete prepared using MSWI bottom ash as aggregates, the products of alkali-silica reaction (ASR) were observed [65], and the cracks induced by the formation of ASR gel were also identified [66]. However, when using MSWI bottom ash as SCM and AAM precursor, it remains unclear whether adding MSWI bottom ash will induce alkali-silica reaction. More research is required in this area.

The chloride content in MBA is 0.27 wt%. This value is much higher than that in FA or BFS. According to the European standard NEN-EN 206 [67], the chloride content in binder may not exceed 1 wt% for concretes without steel reinforcement or other metal embedment. For reinforced and pre-stressed concretes, the maximum chloride content in binder is restricted to 0.2 wt%. Given that the Cl content of MBA is slightly higher than 0.2 wt%, it is suitable to use MBA as binder materials in non-reinforced concretes. For the application of reinforced concretes, the risk of steel reinforcement corrosion induced by the Cl in MBA can be mitigated by reducing the percentage of MBA in the binder.

3.1.2. Mineralogical composition

The contents of the reactive crystalline phases and the amorphous phase determine the reactivity of MBA. Fig. 3 (a) presents the XRD spectrum of MBA. This figure shows that quartz is the primary crystalline phase in MBA. Besides, the peaks of silicates and calcite are also identified in the spectrum of MBA. The silicates detected include gehlenite, albite, orthopyroxene, diopside, and wollastonite. Table 6 lists the formulae and the Inorganic Crystal Structure Database (ICSD) codes of all the crystalline phases found in MBA. The proportion of each phase, as determined by the QXRD analysis, is also presented in the same table. The mineralogical composition of MBA is similar to the MSWI bottom ash investigated in previous studies [28]. According to the QXRD analysis, quartz accounts for the largest proportion (12.1 wt%) among all the crystalline phases. The second major crystalline phase in MBA is diopside, with its content of 4.4 wt%. Except for diopside, the contents of other silicates are all below 3 wt%. The content of calcite is around 2.1 wt%. Phases like halite, corundum, goethite, gibbsite, and iron are present in trace amounts (<1 wt%).

The diffraction pattern of MBA also illustrates the "hump" feature. By enlarging the area marked in Fig. 3 (a), a broad hump centered at a 2θ angle of 32.5° between 25° and 40° can be observed in Fig. 3 (b). As presented in Table 6, the amorphous phase in MBA reaches 68.1 wt%. The quantity of the amorphous phase in MBA is slightly lower than in FA, but much lower than in BFS. As illustrated in Fig. 4 (a) and (b), the broad amorphous hump can be easily recognized in the spectra of FA and BFS. In the XRD patterns of FA and BFS, the hump centered at 2θ of 22.5° and 30°, respectively. Unlike entirely amorphous BFS, FA contains crystal phases, mainly quartz and mullite. The QXRD analysis results indicate that FA has 11.5 wt% quartz and 11.7 wt% mullite (Table 7). The amorphous phase makes up 74 % of the total weight of FA.

Fig. 3 (c) shows the XRD spectrum of the insoluble residue obtained after the dissolution treatments of MBA. The hump representing the amorphous phase is not found in Fig. 3 (c), indicating that the amorphous phase in MBA was dissolved during the chemical dissolution treatments. This observation further confirms the presence of amorphous phase in MBA. According to the results of XRF analysis, the insoluble residue mainly consists of SiO_2 (70.5 wt%), Al_2O_3 (12.5 wt%), CaO (5.5 wt%), Fe_2O_3 (3.8 wt%), and MgO (2.5 wt%). In the XRD pattern of the insoluble residue, mainly the peaks of quartz, augite, and wollastonite are observed. Quartz and wollastonite are the phases of MBA that remained undissolved after the chemical dissolution tests, while augite ($CaMg_{0.6}Fe_{0.2}Al_{0.7}Si_{1.5}O_6$, ICSD 16905) is the newly formed crystalline phase. The mass of MBA decreased by 78.5 % due to dissolution treatments, higher than the amorphous phase content calculated by the QXRD analysis (68.1 wt%). This is because part of the mass loss is caused by the dissolution of the crystalline phases during the chemical dissolution treatments of MBA.

3.1.3. Chemical composition of amorphous phase

When MBA is used as SCM and AAM precursor, it is necessary to

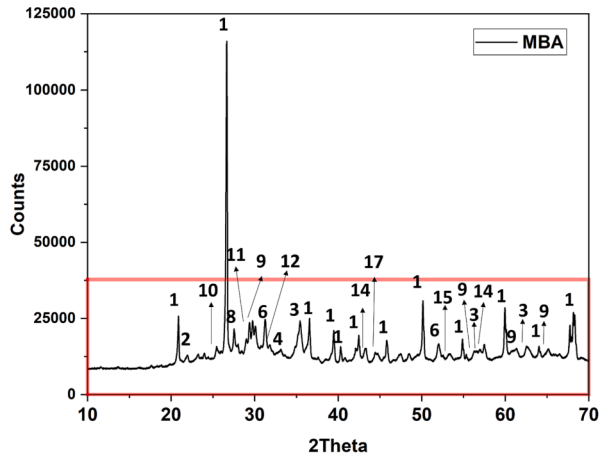

(a) XRD pattern of MBA

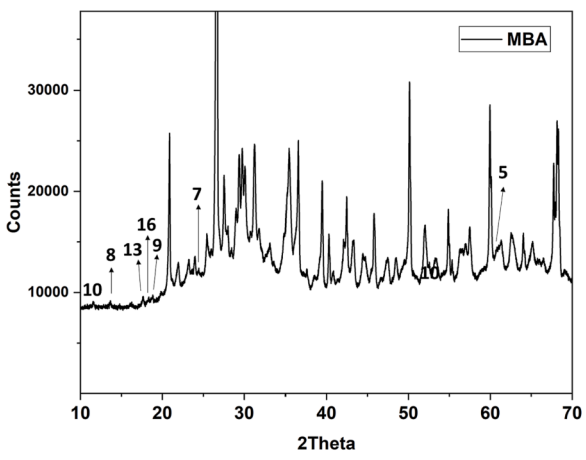

(b) Enlarged area in the XRD pattern of MBA

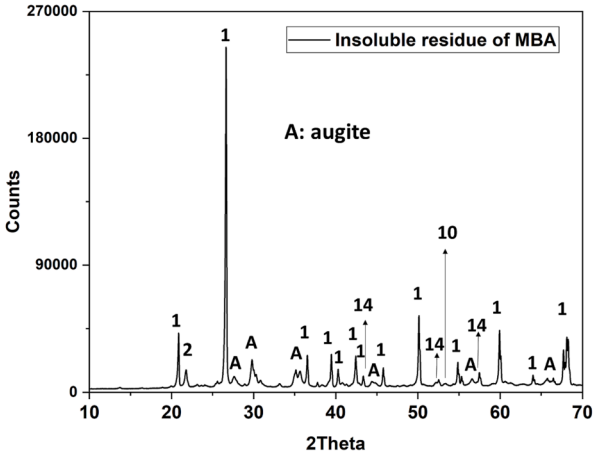

(c) XRD pattern of the insoluble residue of MBA

Fig. 3. (a) XRD spectrum of MBA. (b) Enlarged image of the area labeled in the XRD spectrum of MBA. (c) XRD spectrum of the insoluble residue of MBA obtained after chemical dissolution treatments. The peak labels follow the labels described in Table 6.

Table 6
Mineral phases present in MBA and QXRD analysis results of MBA.

Phases	Proportions (wt.%)	Labels	Formulae	ICSD codes
Quartz	12.1	1	SiO_2	541,929
Cristobalite	0.4	2	SiO_2	1,251,919
Magnetite	0.9	3	Fe_3O_4	92,356
Hematite	0.4	4	Fe_2O_3	453,828
Wustite	0.2	5	FeO	309,924
Gehlenite	2.8	6	$Ca_2Al_2SiO_7$	1,411,155
Albite	1.9	7	$NaAlSi_3O_8$	1,402,109
Orthopyroxene	1.4	8	$Ca_{0.02}Mg_{0.30}Fe_{0.68}SiO_3$	1,615,622
Diopside	4.4	9	$CaMg_{0.69}Fe_{0.31}Si_2O_6$	77,809
Wollastonite	2.6	10	$CaSiO_3$	1,253,098
Calcite	2.1	11	$CaCO_3$	1,611,066
Halite	0.4	12	NaCl	311,644
Phosphammite	1.1	13	$H(NH_4)_2(PO_4)$	1,401,715
Corundum	0.7	14	Al_2O_3	527,601
Goethite	0.4	15	FeO(OH)	71,810
Gibbsite	0.2	16	$Al(OH)_3$	1,005,040
Iron	0.1	17	Fe	1,503,158
Amorphous phase	68.1	–	–	–
Sum	100	–	–	–

determine the chemical composition of the amorphous phase in MBA. The amorphous phase is the primary reactive phase in MBA, and its chemical composition can influence the reaction product formation. Table 8 lists the chemical composition of the amorphous phase in MBA, FA, and BFS. The percentages are absolute values and are presented without normalization. As shown in Table 8, SiO_2 is the primary component (34.2 wt%) in the amorphous phase of MBA. In terms of CaO, Al_2O_3, Na_2O, Fe_2O_3, and MgO, the content of each compound is less than 10 wt%. It is worth noting that the SiO_2 content calculated for the amorphous phase of MBA in the QXRD analysis is slightly lower than the reactive silica content (37.77 wt%) determined by the chemical dissolution treatments. One possible explanation is that the chemical dissolution treatments overestimate the content of the amorphous phase in MBA, resulting in a higher value of the reactive silica content.

Compared with FA, MBA contains less SiO_2 in the amorphous phase. The SiO_2 content in the amorphous phase of MBA is almost equal to that in BFS. The CaO content in the amorphous phase of MBA is 8.8 wt%, which is about one-fourth of its content in BFS but twice the content found in FA. The Al_2O_3 content in the amorphous phase of MBA is 7.9 wt %, only around half of that in the amorphous phase of FA or BFS. Besides, much more Na_2O was found in the amorphous phase of MBA (3.8 wt%) than in FA or BFS (lower than 1 wt%). The amount of Fe_2O_3 in the amorphous phase of MBA is also higher than that in FA and BFS. In terms of the MgO content, MBA has 1.7 wt% MgO, much lower than BFS.

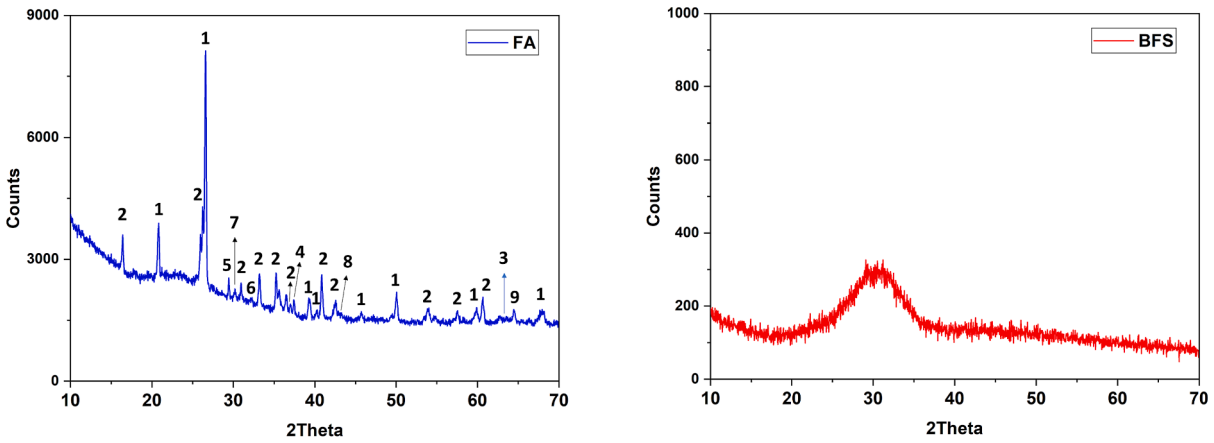

(a) XRD pattern of FA (b) XRD pattern of BFS

Fig. 4. (a) XRD spectrum of FA. The peak labels follow the labels defined in Table 7 (b) XRD spectrum of BFS.

Table 7
Mineral phases present in FA and QXRD analysis results of FA.

Phases	Proportions (wt.%)	Labels	Formulae	ICSD codes
Quartz	11.5	1	SiO_2	156,198
Mullite	11.7	2	$Al_{2.24}Si_{0.76}O_{4.88}$	313,794
Hematite	0.5	3	Fe_2O_3	2,070,090
Lime	0.1	4	CaO	1,503,123
Calcite	0.2	5	$CaCO_3$	1,611,066
Hexapotassium hexaoxodiferrate	0.1	6	$K_6(Fe_2O_6)$	16,534
Iron(III) oxide hydroxide	1.3	7	FeO(OH)	94,874
Periclase	0.3	8	MgO	1,110,749
Wadsleyite	0.3	9	$Mg_{1.84}Fe_{0.16}SiO_4$	66,491
Amorphous phase	74.0	–	–	–
Sum	100	–	–	–

Table 8
Chemical composition of amorphous phase in MBA, FA, and BFS, calculated by subtracting the percentages of the elements in crystalline phases from the chemical compositions of MBA, FA, and BFS.

Compounds	Percentages in the amorphous phase (wt.%)		
	MBA	FA	BFS
SiO_2	34.2	41.3	35.0
CaO	8.8	4.3	36.3
Al_2O_3	7.9	15.7	14.3
Fe_2O_3	6.2	5.1	0.4
Na_2O	3.8	0.9	0.2
K_2O	0.8	1.6	0.5
MgO	1.7	0.9	9.42
Others	4.7	4.2	3.9
Sum	68.1	74.0	100

3.1.4. Composition difference between the amorphous phase and the glass in MBA

Given that waste glass is one of the major sources of the amorphous phase in MBA, it is necessary to examine whether the amorphous phase of MBA and the glass particles in MBA have the same composition. The XRD spectrum in Fig. 5 (a) proves that these manually selected glass particles are almost 100 % amorphous. The QXRD analysis results indicate that these glass particles only contain 1 wt% quartz. The hump representing the amorphous phase appeared in the XRD spectrum of the glass particles at the same location as that observed in the XRD spectrum of MBA (Fig. 3 (a)).

The chemical composition of the glass particles in MBA is illustrated in Fig. 5 (b). The main components in the glass particles are SiO_2 (70.2 wt%), Na_2O (12.9 wt%), and CaO (10.7 wt%). This chemical composition is almost the same as that of the soda-lime glass used in the production of glass containers and glass windows [68]. In the SiO_2-CaO-Al_2O_3 and the SiO_2-Na_2O-Fe_2O_3 ternary diagram, the location of the dot representing the composition of glass particles does not overlap with the dot of the amorphous phase in MBA (see Fig. 6 (a) and (b)). This observation indicates that the chemical composition of the glass particles is quite different from the chemical composition determined in the amorphous phase in MBA. In addition to soda-lime glass, other amorphous phases containing CaO, Al_2O_3, and Fe_2O_3 are also present in MBA.

3.1.5. Relative contents of SiO_2, CaO, and Al_2O_3 in the amorphous phase of MBA

The chemical composition of the amorphous phase in MBA was compared with the chemical composition of the amorphous phase in Class F coal fly ash and blast furnace slag reported in the literature. The reference data collected for Class F coal fly ash are the chemical composition of the amorphous phase [69–76]. The reference data collected for blast furnace slag are the XRF results [49–103]. There are two reasons for this choice. First, the information about the composition of the amorphous phase is very limited in the literature. Second, blast furnace slag usually contains more than 90 % amorphous phase [132,133]. The XRF results of blast furnace slag primarily reveal the chemical composition of the amorphous phase. As shown in the SiO_2-CaO-Al_2O_3 ternary diagram (Fig. 6 (a)), the chemical compositions of the amorphous phase in FA and BFS used in this work are typical for Class F coal fly ash [69–76] and blast furnace slag [49–103]. The dot representing the relative contents of SiO_2, CaO, and Al_2O_3 in the amorphous phase of MBA is within the same region as that in the amorphous phase of Class F coal fly ash reported in the literature [69–76].

The mass ratio of CaO/SiO_2 in the amorphous phase of blast furnace slag is usually used as an indicator to assess its reactivity as AAM precursor [133]. BFS with higher CaO/SiO_2 usually has a more depolymerized and disordered structure, resulting in a higher reactivity for the application of AAM precursor [134–136]. As demonstrated in Fig. 7, the CaO/SiO_2 ratio of MBA (0.3) is much lower than that of BFS (1.0), suggesting that the reactivity of MBA is much lower than that of BFS. In the case of coal fly ash, the mass ratio between SiO_2/Al_2O_3 in the amorphous phase can be used to indicate its reactivity as AAM precursor [133]. As shown in Fig. 7, the SiO_2/Al_2O_3 ratio for the amorphous phase of MBA is 4.3, almost two times that in the amorphous phase of FA. The aluminosilicate glass with its SiO_2/Al_2O_3 ratio within the range of 2 to 4 was found to be a suitable precursor for alkali-activated materials [137–143]. Unlike FA, the SiO_2/Al_2O_3 ratio of the amorphous phase in

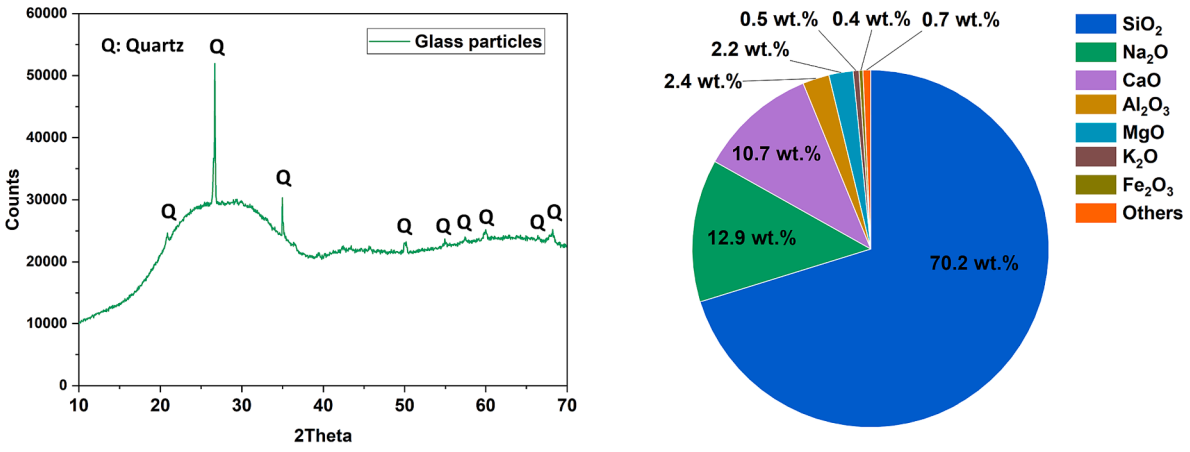

(a) XRD pattern of waste glass particles in MBA (b) XRF analysis results of glass paritilces in MBA

Fig. 5. (a) mineralogical composition (determined by XRD analysis) and (b) chemical composition (determined by XRF analysis) of the glass particles shown in Fig. 2 (b).

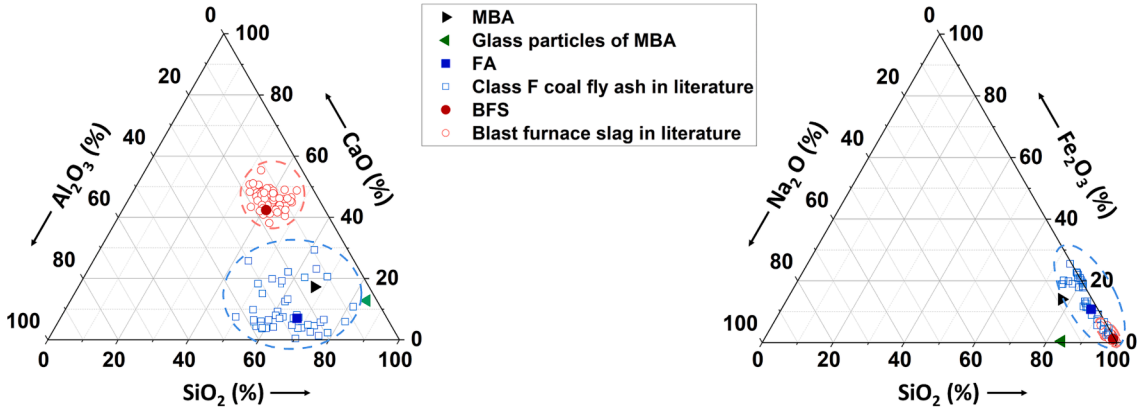

(a) SiO_2-CaO-Al_2O_3 ternary diagram (b) SiO_2-Na_2O-Fe_2O_3 ternary diagram

Fig. 6. (a) Ternary diagram showing the relative content of SiO_2, CaO, and Al_2O_3 in the amorphous phase of MBA, BFS, FA, and glass particles of MBA (b) Ternary diagram showing the relative content of SiO_2, Na_2O, and Fe_2O_3 in the amorphous phase of MBA, BFS, FA, and glass particles of MBA. The data of the amorphous phase of Class F coal fly ash are collected from the literature [69–76]. The composition information of blast furnace slag is from the literature [77,78,87–96,79,97–106,80,107–116,81,117–126,82,127–131,83–86]. The ternary diagrams are plotted according to the weight percentages of the oxides.

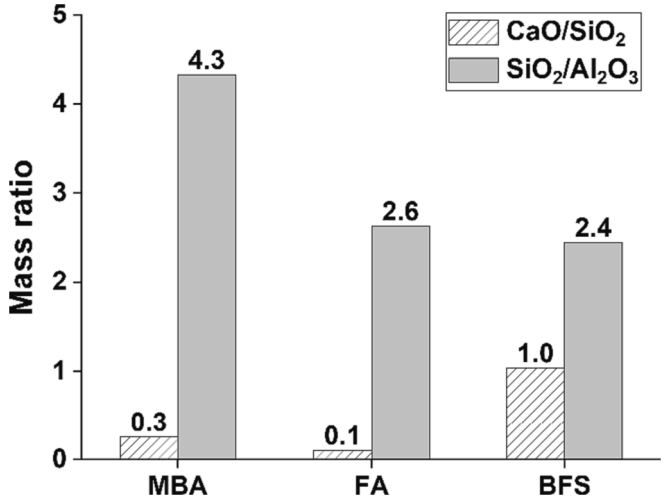

Fig. 7. Mass ratio of CaO/SiO_2 and SiO_2/Al_2O_3 calculated for the amorphous phase in MBA, BFS, and FA.

MBA is not within the desirable range.

3.1.6. *Reactivity of MBA as SCM*

The information about the pozzolanic reactivity of MBA can be used in the mix design of blended cement pastes. The reactivity of MBA as SCM was studied by measuring the hydration heat evolution of R^3 pastes. The calorimetry test results of the R^3 pastes prepared with MBA, FA, or BFS are presented in Fig. 8 (a). The cumulative heat collected after different time intervals is shown in Fig. 8 (b). After 7 days of reaction, the cumulative heat generated by MBA is only one-third of that by BFS, but slightly more than that of FA. These results indicate that MBA is much less reactive than BFS but could be as reactive as FA.

The difference in the heat release between MBA and FA is significant during the first 3 days (Fig. 8 (a)). Afterward, this heat release difference decreased, reaching the lowest value at 7 days. The big difference observed at early ages (<3 days) can be attributed to the intensive oxidation of the residual metallic Al in MBA. The residual metallic Al in MBA reacts readily with $Ca(OH)_2$, which is introduced excessively in the R^3 pastes [46]. The oxidation of the metallic Al is expected to finish within 1 day [144].

At room temperature, in the alkaline solution, metallic Al first reacts with water to form $Al(OH)_3$ and H_2, then $Al(OH)_3$ reacts with OH^-.

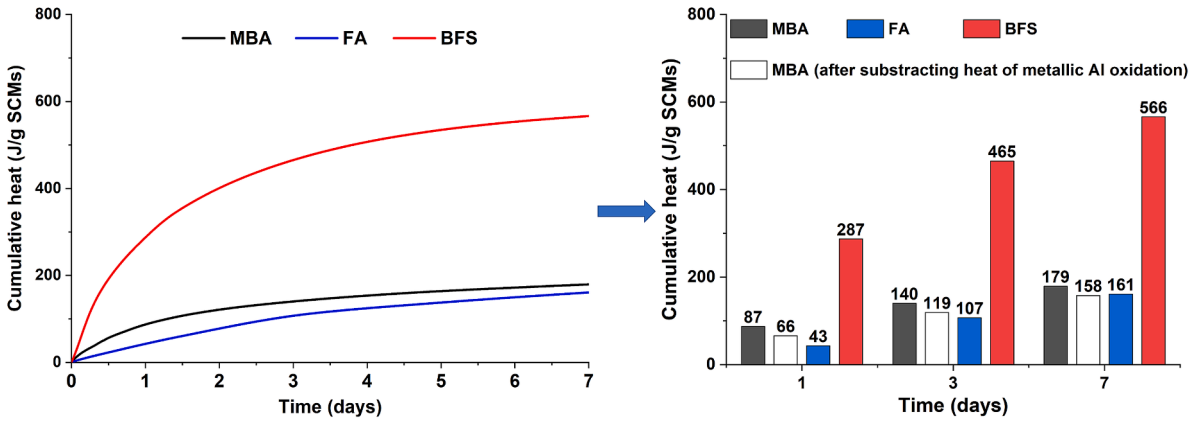

(a) Calorimetry test results (b) Cumulative heat for 1 day, 3 days, and 7 days

Fig. 8. (a) Calorimetry test results of the R^3 pastes prepared with MBA, FA, or BFS. The results are expressed as J/g of SCMs. (b) Cumulative heat collected after different time intervals.

Theoretically, the reaction of 1 g of metallic Al with water generates 16.3 kJ of heat ($2Al + 6H_2O \rightarrow 2Al(OH)_3 + 3H_2$) [145]. The mass of metallic Al in 1 g of MBA is 0.0013 g. In this case, the reaction heat contributed by the reaction between metallic Al and water in the calorimetry test of MBA would be 21 J. As shown in Fig. 8 (b), after subtracting the reaction heat of metallic Al, the heat released by the reaction of the reactive minerals in MBA is around 158 J, almost the same as the 7-day heat of FA (161 J). It can be concluded that as SCM, the reactivity of MBA is similar to FA.

3.1.7. Reactivity of MBA as AAM precursor

The reactivity of MBA as AAM precursor was assessed via dissolution tests. The dissolution tests mimic the dissolution of precursors in the pore solution. Analysis of the dissolution behavior of MBA provides information about the elements that participate in the formation of reaction products and delivers a fundamental understanding of the early-age reaction. The concentrations of Si, Al, Ca, Fe, and Mg (hereafter denoted as [Si], [Al], [Ca], [Fe], and [Mg], respectively) in the filtrated solution are shown in Fig. 9. This solution was obtained after dissolving MBA, FA, or BFS in NaOH solution for 24 h.

3.1.8. Concentrations of dissolved elements

- **[Si], [Al], and [Ca]**

As shown in Fig. 9, the filtrate of MBA, FA, and BFS is enriched with Si and Al. Regardless of the concentration of the NaOH solution, MBA and FA released much less Si and Al than BFS. Compared with MBA and FA, the amorphous phase of BFS with higher CaO/SiO_2 has a more depolymerized and disordered structure [134] and dissolves more easily in alkaline solution. Accordingly, the reactivity of MBA and FA is much lower than that of BFS. The high [Si] and [Al] in the filtrate of BFS indicates that a large amount of BFS has been dissolved.

Given that the mass ratio between SiO_2 and CaO in the amorphous phase of BFS is one, the [Ca] in the filtrate of BFS is expected to be in the same range as [Si]. However, the [Ca] in the filtrate of BFS is much lower than [Si]. When 4 M NaOH solution was used in the dissolution test, the [Ca] in the filtrate of BFS was higher than that in the filtrate of MBA and FA. Further increasing the concentration of NaOH solution to 5 M or 6 M, the [Ca] in the filtrate of BFS decreased and was similar to that in the filtrate of MBA and FA.

The low [Ca] in the filtrate of BFS can be attributed to the formation of Ca-bearing phases, such as $Ca(OH)_2$, C-S-H gel, and C-A-S-H gel. Although a large liquid-to-solid ratio is used to prevent the precipitation of reaction products, there exists a concentration gradient in the vicinity of the surface of BFS particles [146]. The [Ca] in the region close to the surface of BFS particles is higher than the bulk solution [146]. As a result, the Ca^{2+} ions in this region could combine with OH^- and form $Ca(OH)_2$ precipitates. In the NaOH solution with a pH higher than 11.5, $Ca(OH)_2$ is thermodynamically more stable than Ca^{2+} ions [147]. Compared with $Ca(OH)_2$, the Ca^{2+} ions are less likely to interact with the silicate and aluminate species to form a C-S-H or C-A-S-H layer on the surface of BFS particles. This is because if Ca^{2+} ions are consumed due to the formation of C-S-H or C-A-S-H gel, the decline of [Si], [Al], and [Ca] in the filtrate should be in the same order of magnitude. In reality, [Ca] is much smaller than [Si] and [Al] in the filtrate of BFS.

The [Si] and [Al] in the filtrate of MBA are higher than in the filtrate of FA, indicating that MBA is more soluble than FA. Considering that the CaO content in the amorphous phase of MBA is around two times that in FA, MBA with higher solubility is expected to release more Ca^{2+} than FA during the dissolution tests. However, the [Ca] in the filtrate of MBA appeared to be in the same range as that in the filtrate of FA. As discussed above, precipitation of Ca^{2+} ions cannot be avoided during the dissolution test. The precipitate formed is more likely to be $Ca(OH)_2$ than the C-S-H gel or C-A-S-H gel. It is possible that the Ca^{2+} ions released by MBA also react with OH^- to form $Ca(OH)_2$, resulting in a low [Ca] in its filtrate.

- **[Fe] and [Mg]**

The [Fe] in the filtrate of MBA is only around one-quarter of [Si]. The [Fe] in the filtrate of MBA is higher than that of FA and BFS. This higher Fe concentration in MBA may be due to the higher Fe_2O_3 content in the amorphous phase of MBA compared with FA and BFS. In the filtrate of MBA, the [Mg] is the lowest (<0.5 mg/l) among the measured elements ([Si], [Al], [Ca], [Fe], and [Mg]). The concentration of Mg remained at a very low level regardless of the molarity of NaOH. Similar phenomena can also be observed for the Mg dissolved from BFS and FA.

3.1.9. Ratio of dissolved Si and Al

The compressive strength of AAM can be used as an indicator of the reactivity of precursors. The AAM prepared with a more reactive precursor usually has a higher compressive strength. Duxson et al. [148] indicated a correlation between the compressive strength of AAM and the Si/Al molar ratio in the mixture of precursor and alkaline activator. When increasing the Si/Al molar ratio from 1.15 to 1.9, the compressive strength of the AAM became higher due to the formation of a more homogeneous and denser microstructure. The optimal Si/Al molar ratio was 1.9 for preparing AAM with aluminosilicate materials [148]. Therefore, the Si/Al molar ratio in the filtrate of MBA, FA, or BFS was

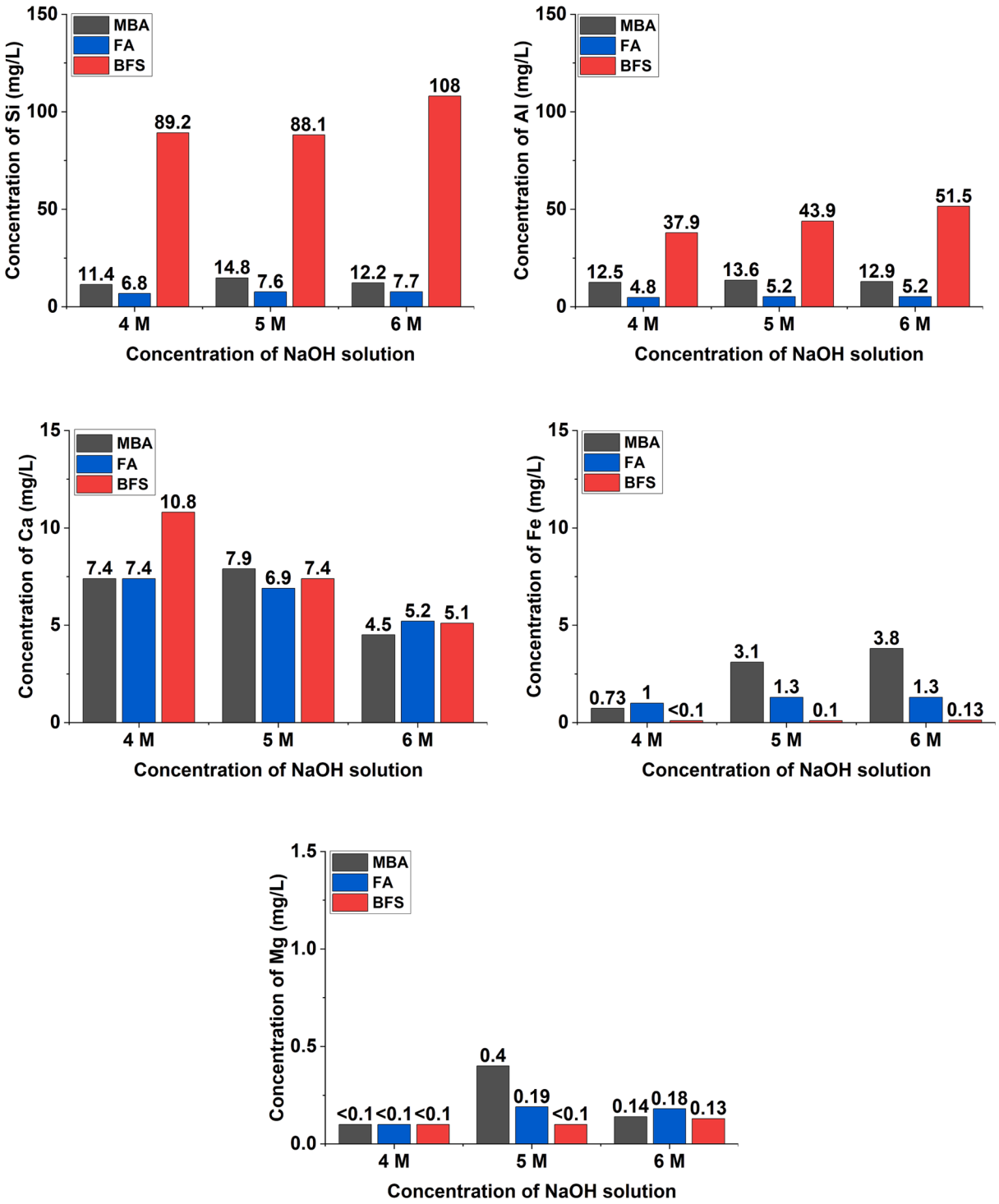

Fig. 9. Element concentrations in the filtrated solution obtained after the dissolution tests of MBA, FA, and BFS in the NaOH solution of 4 M, 5 M, and 6 M (M: molarity).

calculated to provide additional insight into the reactivity of these precursors and the mix design of AAM.

As illustrated in Fig. 10, the Si/Al molar ratio in the filtrate of MBA fluctuates around 0.9, lower than the ratio in the filtrate of FA and BFS. The molar ratio of Si and Al released by MBA is far below the optimal value found by Duxson et al. [148]. This low Si/Al molar ratio is not favorable for the strength development of alkali-activated MBA at an early age. In our preliminary research, alkali-activated MBA paste did not harden within 24 h at room temperature when NaOH solution (4 M) was used as activator. The hardened paste samples can be obtained after increasing the Si content in the AAM system by adding water glass to the activating solution. Therefore, when MBA is used to prepare AAM, it is recommended to increase the Si/Al ratio in the mixture of precursor and activator by adding Si-enriched precursors or Na_2SiO_3 solution.

3.1.10. Thermodynamic modeling of the reactions in alkali-activated MBA paste

Thermodynamic modeling was used to predict the solid phase assemblages and the pore solution in alkali-activated MBA paste. The modeling results provide insight into the evolution of the reaction

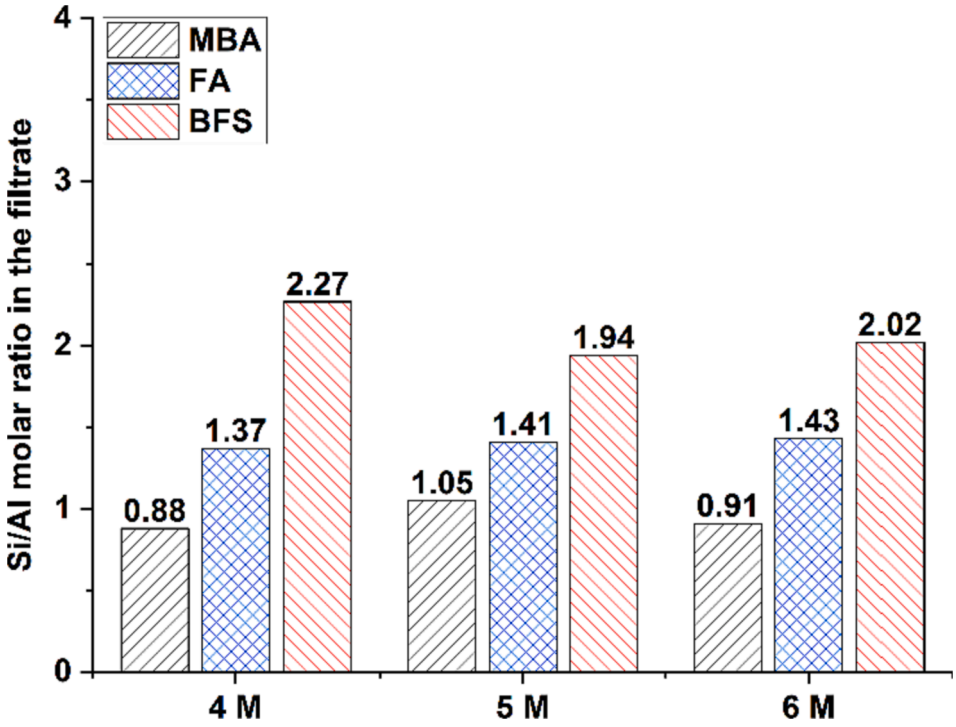

Fig. 10. Si/Al molar ratio in the filtrate, calculated using the dissolution test results presented in Fig. 9 (M: molarity).

products and the pore solution in alkali-activated MBA paste when the Na_2O content in the activating solution changes from a low level (2 wt%) to a high level (10 wt%). This information can also be used as a rough guide to the mix design, making it possible to control the reaction product formation and tailor the properties of MBA-based AAM.

3.1.11. *Total amount of reaction products*

The amount of reaction products that can form upon alkali activation is strongly influenced by the proportions of reactive phases (mainly the amorphous phase) in AAM precursors. MBA contains less amorphous phase than FA and BFS (see Table 8), suggesting that the reaction products formed in alkali-activated MBA paste would be less than that in alkali-activated FA paste and alkali-activated BFS paste. Fig. 11 presents the solid phase assemblages predicted by thermodynamic modeling in alkali-activated MBA paste, alkali-activated FA paste, and alkali-activated BFS paste. According to the prediction, the reaction products obtained after activating 100 g BFS with NaOH solution would be much more than those obtained from the reaction of 100 g MBA or 100 g FA. Compared with alkali-activated FA paste, the mass of reaction products formed in alkali-activated MBA paste would be slightly lower.

Apart from the reaction products, Fig. 11 also shows that the un-reactive fraction in MBA is larger than in FA and BFS. The un-reactive fraction illustrated in Fig. 11 refers to the crystalline phases and part of the amorphous phase. In the modeling, only the components including SiO_2, CaO, Al_2O_3, Fe_2O_3, Na_2O, K_2O, and MgO of the amorphous phase were assumed to participate in reaction product formation. The remaining components of the amorphous phase were considered to be unreactive. Regarding the pore solution, its mass in alkali-activated MBA paste was forecast to be roughly equivalent to that of alkali-activated FA paste but much larger than that of alkali-activated BFS paste (Fig. 11).

3.1.12. *Predicted solid phase assemblages*

It is meaningful to predict the gel phases that can form in alkali-activated MBA. This information can be used as a reference when designing MBA-based AAM mixtures. The nanostructure of the gel phases formed in alkali-activated materials has a significant effect on the mechanical properties of synthesized alkali-activated materials [149]. According to thermodynamic modeling (Fig. 11 (a)), the major reaction products formed after MBA reacting with NaOH solution are C-(N-)A-S-H gel, N-(C-)A-S-H gel, and zeolite. The details about the chemical compositions of predicted C-(N-)A-S-H gel and N-(C-)A-S-H gel can be found in Appendix A. The zeolite minerals predicted in alkali-activated MBA paste include natrolite ($Na_2Al_2Si_3O_{10}{\cdot}2H_2O$) and Ca-chabazite ($Ca_{0.111}Al_{0.111}Si_{0.778}{\cdot}0.667H_2O$). The mass of C-(N-)A-S-H gel shows little changes with the increase of the Na_2O in the NaOH solution. When the Na_2O content was higher than 4.5 wt%, the amount of N-(C-)A-S-H gel in alkali-activated MBA paste started to decrease with the increase of Na_2O content. Meanwhile, more natrolite was expected to be found in alkali-activated MBA paste [150]. The Ca-chabazite was forecast to form only when the Na_2O content was lower than 2.5 wt%.

The prediction about the solid phase assemblages in alkali-activated MBA paste at the Na_2O content of 10 wt% agrees with the experimental results reported by Maldonado-Alameda et al. [57]. The MSWI bottom ash used by Maldonado-Alameda et al. [32,57] has a chemical composition (determined by XRF) and amorphous phase content (determined by QXRD analysis) falling within the same range as that of MBA. In their work, the 28-day alkali-activated MSWI bottom ash paste was prepared using an activator containing 9.7 wt% Na_2O with SiO_2/Na_2O molar ratio of 2.9. In the synthesized paste specimen, the C-(A)-S-H gel, N-A-S-H gel, and zeolite were all identified. The total amount of N-A-S-H gel, zeolite, and C-(A)-S-H dissolved in HCl extraction was 59.9 wt%. The amount of C-(A)-S-H gel was around 33.5 wt%, as determined by the salicylic acid/methanol (SAM) extraction. By subtracting the amount of C-(A)-S-H gel dissolved by HCl extraction, the total amount of N-A-S-H gel and zeolite is around 26.4 wt%. The mass ratio between C-A-S-H gel and the sum of N-A-S-H gel and zeolite is 1.26. This value is slightly higher than 0.95, the mass ratio predicted by thermodynamic modeling at the Na_2O content of 10 wt%. This discrepancy in the mass ratio may be due to the difference in the SiO_2 content in the activator.

The types of zeolite phases predicted in alkali-activated MBA paste are the same as those in alkali-activated BFS paste. The Ca-chabazite and natrolite formed in alkali-activated BFS paste are expected to be much less, only in trace amounts. According to the modeling results, the alkali

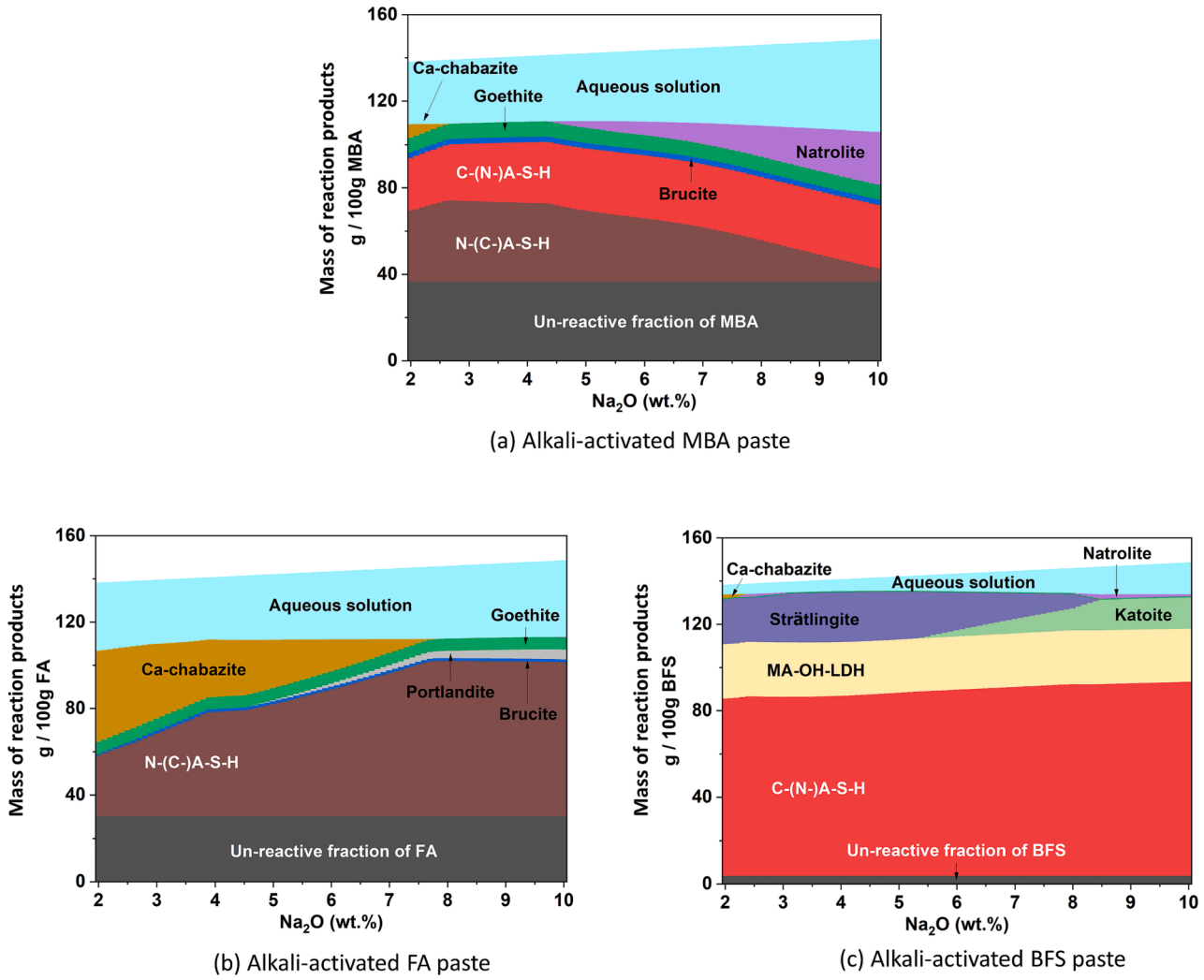

Fig. 11. Thermodynamically simulated phase assemblage, solid reaction product mass, and pore solution mass after activating 100 g MBA, 100 g FA, or 100 g BFS with NaOH solution. The simulation was performed with GEMS-Selektor v.3 [52,53]. The data is presented as a function of the Na_2O content in the activator. The percentage of Na_2O is with respect to the mass of the precursor.

activation of FA only leads to the formation of Ca-chabazite, and its content decreases with the increase in the Na_2O content. Previous researchers also detected zeolite minerals in alkali-activated MSWI bottom ash. However, instead of Ca-chabazite and natrolite, the zeolite mineral found in literature was gismondine ($CaAl_2Si_2O_8{\cdot}4H_2O$) [57]. This zeolite mineral was formed after the MSWI bottom ash reacted with a mixture of NaOH and Na_2SiO_3 solution for 28 days. In the activator, the Na_2O content was 10.7 wt% with respect to the content of MSWI bottom ash, and the SiO_2/Na_2O molar ratio was 2.6 [57].

The minor reaction products in alkali-activated MBA paste were predicted to be goethite (FeO(OH)) and brucite ($Mg(OH)_2$). These two phases with small quantities were also likely to form in alkali-activated FA paste. The formation of goethite and brucite could be attributed to the existence of Fe_2O_3 and MgO in the amorphous phase of MBA (Table 8). However, the detection of these two phases in alkali-activated MSWI bottom ash is rarely reported in the literature. It is worth mentioning that the primary crystalline reaction products of alkali-activated BFS paste, including katoite ($3CaO{\cdot}Al_2O_3{\cdot}6H_2O$), strätlingite ($2CaO{\cdot}Al_2O_3{\cdot}SiO_2{\cdot}8H_2O$), and hydrotalcite-like phases (MA-OH-LDH), were not expected to form in alkali-activated MBA paste. Portlandite, the reaction product of alkali-activated FA paste, was not likely to form after MBA reacted with NaOH solution.

3.1.13. *Predicted pore solution*

The prediction of the pore solution in alkali-activated MBA paste can help people understand the role of MBA in the formation of reaction products. Fig. 12 provides information about the simulated pore solution of alkali-activated MBA paste, alkali-activated FA paste, and alkali-activated BFS paste. The concentrations of Al, Ca, Fe, and Mg in the pore solution were forecast to be very small (close to zero) for alkali-activated MBA paste, alkali-activated FA paste, and alkali-activated BFS paste. This prediction indicates that most of these elements released by MBA, FA, and BFS were incorporated into the reaction products. The main differences in the pore solution of these three AAM systems were predicted to lie in the pH and the concentrations of Na and Si.

The alkalinity of the pore solution affects the leaching of heavy metals [151] and the long-term stability of calcium-aluminosilicate hydrates [152] and alkali-aluminosilicate gels [153] in AAM. Therefore, it is useful to predict the pH of the pore solution in alkali-activated MBA paste. As shown in Fig. 12, the pH of the pore solution of alkali-activated BFS paste was expected to be the highest (14.43 to 14.92). The predicted alkalinity in the pore solution of alkali-activated MBA paste, ranging from 13.8 to 14.74, was higher than that of alkali-activated FA paste, between 9.17 and 14.48. This difference in predicted pH of pore solution could be explained by the CaO content difference in the amorphous phase of precursors. The CaO content in the

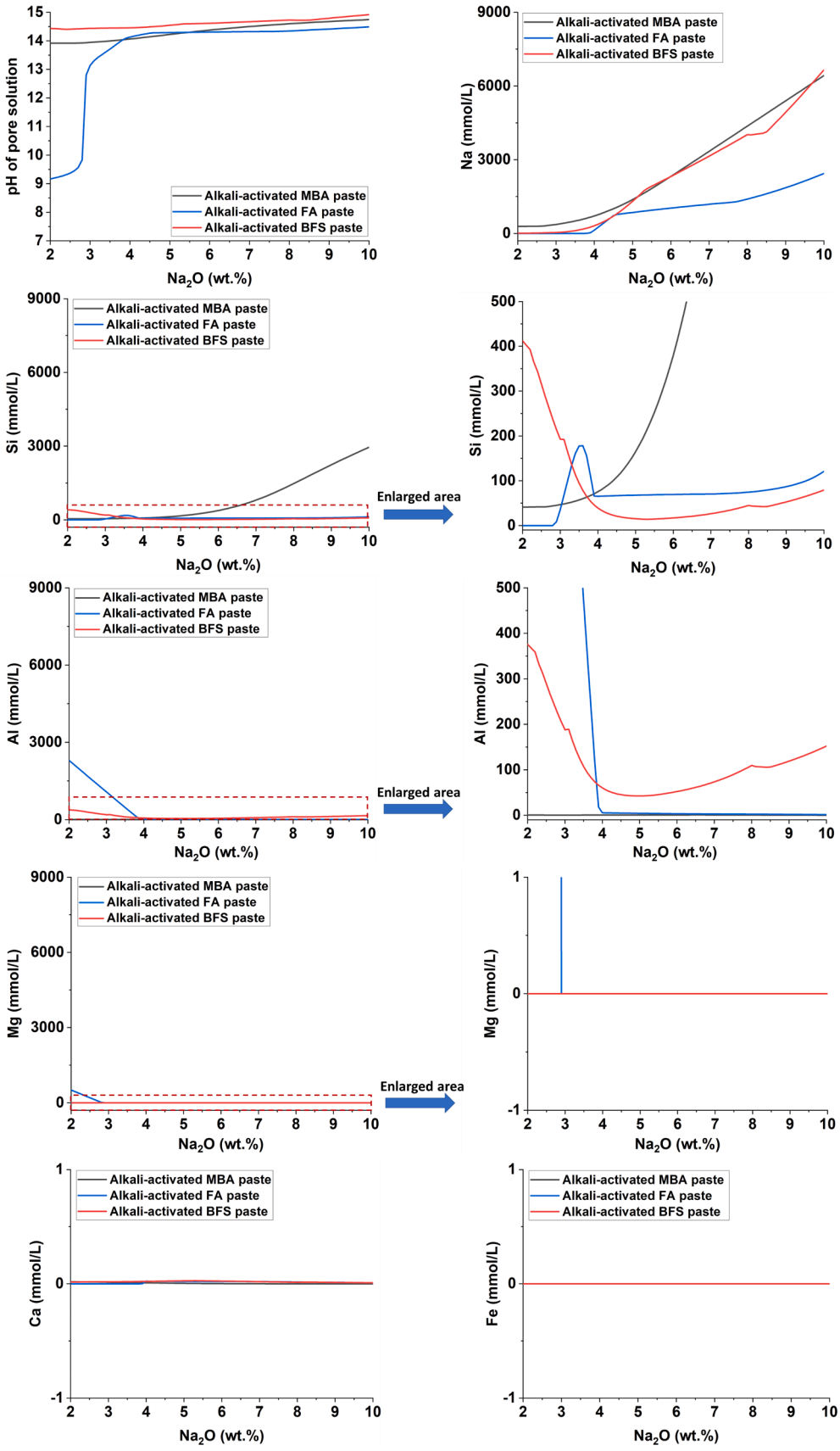

Fig. 12. Simulated pH of the pore solution and simulated concentration of Na, Si, Al, Ca, Fe, and Mg in the pore solution. The data is presented as a function of the Na_2O content in the activator. The percentage of Na_2O is with respect to the mass of the precursor.

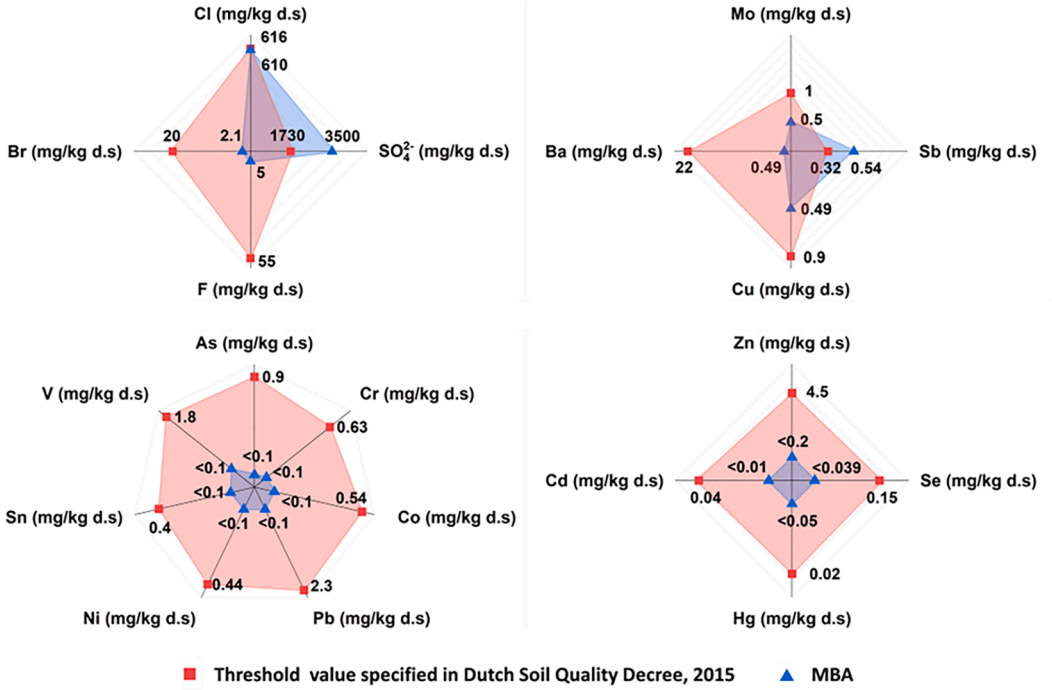

Fig. 13. The quantities of soluble constituents leached from MBA and the threshold values specified in the Dutch Soil Quality Decree, 2015 [63]. The unit is in mg/kg of dry matter (d.s).

amorphous phase, from the largest to the smallest, was in the following order: BFS, MBA, and FA. This order was the same as that of the predicted pH of the pore solution in synthesized alkali-activated materials. This finding was consistent with the thermodynamic modeling results reported by Xiao et al. [35]. When the Na_2O content in the activator was fixed, increasing the CaO content of the amorphous phase would also increase the pH of the pore solution [35].

Fig. 12 shows the predicted concentrations of Na in the pore solution of alkali-activated MBA paste, alkali-activated FA paste, and alkali-activated BFS paste. The Na concentration in the pore solution of alkali-activated MBA paste was forecast to be slightly higher than that of alkali-activated BFS paste. The pore solution of alkali-activated FA paste was predicted to have the lowest Na concentration. The concentration of Na in the pore solution AAM would increase due to the release of Na after the dissolution of precursors. The Na_2O content in the amorphous phase of MBA (3.8 wt%) is much higher than that in FA and BFS. The Na dissolved from MBA could be much more than FA and BFS, dramatically increasing the Na concentration in the pore solution.

It is worth noting that the Na_2O content in the amorphous phase of FA (0.9 wt%) is much higher than that in BFS (0.2 wt%). However, the Na concentration in the pore solution of alkali-activated FA paste is lower than that of alkali-activated BFS paste. One possible explanation for the lower Na concentration in the pore solution of alkali-activated FA paste can be that more Na was incorporated in the Na-bearing reaction products. The Na concentration would decrease when the Na in the pore solution was consumed in the reaction product formation. As predicted by the thermodynamic modeling, the N-(C-)A-S-H gel formed after the alkali activation of FA was more than that obtained from the reaction of MBA and BFS (Fig. 11).

In the pore solution of alkali-activated MBA paste, the concentration of Si was forecast to become higher with the increase of Na_2O content in the activator. When the Na_2O content exceeds 4 wt%, the concentration of Si in the pore solution of alkali-activated MBA paste is the highest among these three AAM systems. The increase in the concentration of Si in the pore solution of alkali-activated MBA paste could be attributed to the reduction in N-(C-)A-S-H gel formation. The Si/Al ratio of the N-(C-)A-S-H gel could reach as high as four. However, at the Na_2O content above 5 wt%, the N-(C-)A-S-H gel mass was predicted to decrease while more natrolite was formed (Fig. 11). The Si/Al molar ratio of natrolite is around 1.5, less than half of that in the amorphous phase of MBA (3.67). In this case, only part of the Si released by the amorphous phase of MBA could be incorporated into the reaction products. The remaining Si could not form stable reaction products with Na. Introducing Ca- or Al-enriched resources into MBA-based AAM is recommended. In this case, the excessive Si and Na in the pore solution can be consumed, forming stable N-(C-)A-S-H gel or C-(N-)A-S-H gel.

3.1.14. *Leaching potential of MBA*

Possible leaching of contaminants from MBA should be checked prior to its application as SCM and AAM. This information is required to guide the mix design and prevent environmental contamination caused by using MBA in construction materials. Fig. 13 provides information about the mass of heavy metals, chloride, bromide, and sulfate leached from 1 kg MBA. Among all the tested constituents, only the leaching of sulfate and antimony (Sb) is above the threshold values specified in the Dutch Soil Quality Decree 2015 [63]. The amount of sulfate and Sb leached from MBA is almost twice the threshold value. The leaching of bromide, fluoride, and most heavy metals is below the allowable level. The amount of Cl released by 1 kg MBA is 610 mg, just below the upper limit set by the Dutch government (616 mg/kg). The Cl detected in the leachate can be traced back to the soluble salt in MBA, as halite (NaCl) was found in the XRD analysis of MBA.

- **Leaching of sulfate**

Sulfate is usually leached from the mineral phases in MSWI bottom ash, such as ettringite and gypsum [154]. However, ettringite and gypsum were not found in the XRD analysis of MBA. The SO_3 content in MBA was lower than FA, BFS, and Portland cement clinker. Given that the SO_3 content determined by XRF analysis is very low (0.7 wt%), the contents of sulfate-containing mineral phases may be too small to be detected. It is worth mentioning that the leaching of sulfate may not be an issue when MBA is used as SCM. The sulfate released by MSWI bottom ash can be immobilized by forming ettringite (AFt) and monosulfate

(AFm) [48].

- **Leaching of antimony**

The excessive leaching of Sb can be attributed to the organic acids (such as humic and fulvic acids) in MBA and the alkalinity of MBA. The organic acids would form mobile organo-metallic complexes with Sb, promoting the leaching of Sb from MBA [155–159]. Tang et al. [48] found that the leaching of Sb is associated with the organics in MSWI bottom ash. The leaching of Sb was reduced after removing the decarboxylation of organic acids from MSWI bottom ash via heat treatment at 400 °C [160]. The end pH of the leachate obtained after the leaching test of MBA is 9.7. Verbinnen et al. [160] performed the leaching test at a liquid-to-solid ratio of 10 L/kg, the same as that used in this research. The leaching of Sb from MSWI bottom ash was highest at the pH between 8 and 10.

Using MBA as SCM would dramatically reduce the leaching of Sb. In cement system, the pore solution is supersaturated with $Ca(OH)_2$. The pH value of the pore solution lies in the range of 12.4–13.5 [161]. Verbinnen et al. [160] found that the leaching of Sb from MSWI bottom ash reached the lowest value at the pH between 12 and 14, which was around one-quarter of the amount of Sb leached at pH of 9. Accordingly, the leaching of Sb under the alkalinity of cement pore solution would be much lower than that at the pH of 9.7. Besides, the Ca^{2+} dissolved by Portland cement clinker could react with Sb released from MBA to form calcium antimonate precipitates [162], which could inhibit the leaching of Sb. The hydration products, such as C-S-H gel and ettringite, could also incorporate the heavy metals released by MSWI bottom ash via physical and chemical adsorption [163,164].

The excessive leaching of Sb would not be an issue when using 100 % MBA to prepare AAM. According to the thermodynamic simulation results illustrated in Fig. 12 (a), the pore solution of alkali-activated MBA paste would have a pH of around 13.8 to 14.74. At this alkalinity, the leaching of Sb from MSWI bottom ash would be very small [160]. The zeolite minerals (including natrolite and Ca-chabazite) predicted to form in alkali-activated MBA paste could function as adsorbents to immobilize heavy metals [165]. The N-(C-)A-S-H gel and C-(N-)A-S-H gel, the predicted reaction products in alkali-activated MBA paste, also have the potential to encapsulate the heavy metals [166,167].

It is recommended to add BFS to MBA-based AAM systems in order to reduce the leaching of contaminants. Blending MBA with BFS can reduce the proportion of MBA in the AAM, decreasing the total amount of heavy metals in the system. Adding BFS also increases the amount of reactive Ca in the MBA-based AAM system, which in turn raises the pH of the pore solution [35] and promotes the formation of calcium antimonate precipitates [162]. In this way, the Sb released from MBA would be immobilized. Since BFS is much more reactive than MBA, the reaction products formed in AAM prepared with blends of BFS and MBA would be more than that in AAM prepared with MBA. The gel phases formed in AAM would contribute to the encapsulation of heavy metals.

3.2. Remarks on using MBA as SCM and AAM precursor

Based on the above analysis of the composition, reactivity, and leaching potential of MBA, the following remarks are made about how to use MBA for the preparation of blended cement pastes and alkali-activated pastes.

- **Quality upgrade treatments of MBA**

It is not recommended to increase the reactivity of MBA by increasing its amorphous phase because the amorphous phase already accounts for 70 wt% in MBA, which is close to the amorphous content in FA. The amorphous phase of MBA is rich in SiO_2 but deficient in CaO and Al_2O_3. Increasing the contents of reactive CaO and Al_2O_3 in MBA is more beneficial to the reactivity enhancement of MBA.

It is possible to use MBA as SCM and AAM precursor even without removing heavy metals and soluble salts. The leaching of contaminants from the construction materials prepared with MBA can be minimized by limiting the addition of MBA to a low level. The reaction products formed in MBA blended cement pastes or MBA-based AAM can immobilize sulfate and Sb released by MBA.

It is important to reduce the metallic Al content in MBA and determine a threshold value before using MBA as SCM and AAM precursor. The metallic Al in MBA will pose risks of volume expansion and strength reduction to pastes prepared with MBA.

- **Mix design of using MBA in blended cement pastes and AAM**

When preparing blended cement pastes and alkali-activated pastes with MBA, previous experience with Class F coal fly ash-based pastes can be used as a reference because the reactivity of MBA is similar to that of FA. However, it is challenging to obtain equivalent compressive strength when the same mix design is used for MBA and FA. The presence of metallic Al in MBA can lead to a strength decrease in MBA-based pastes.

The content of alkalis and Cl in MBA exceeds the acceptable upper limits in Portland cement clinker. A threshold value for the dosage of MBA in the binder of steel-reinforced concretes should be specified to prevent the risk of steel corrosion. When using MBA in the binder of concretes, the total amount of alkalis in the system should be controlled to avoid the alkali-silica reaction caused by excessive addition of MBA.

According to the dissolution test results of MBA, the molar ratio of dissolved Si/Al is much lower than the optimal value (1.9), indicating that alkali-activated MBA may have low early-age strength. For the mix design of MBA-based AAM, it is recommended to add an appropriate amount of water glass or more reactive Si-enriched precursors to the MBA-based AAM system to increase the early-age strength.

The results of thermodynamic modeling indicate that when the Na_2O content in the activator is higher than 5 wt%, some of the Si released by MBA cannot form stable reaction products with the Na provided by the activator. This information needs to be considered when designing the mix of MBA-based AAM. The Na_2O content in the activator may not exceed 5 wt% to ensure that all the Si released by MBA is incorporated into the reaction products. If the Na_2O content in the activator is set to be higher than 5 wt%, it is recommended to add Ca- or Al-enriched precursors, such as blast furnace slag, to MBA-based AAM. Adding Ca- or Al-enriched precursors can promote gel formation by consuming Si dissolved from MBA, resulting in a strength increase of MBA-based AAM. The Ca^{2+} dissolved from Ca-enriched precursors could also facilitate the immobilization of Sb by forming calcium antimonate precipitates.

4. Conclusions

In this work, the reactivity and leaching potential of MSWI bottom ash powder (MBA) as supplementary cementitious material (SCM) and precursor for alkali-activated materials (AAM) were studied. Based on the experimental results and analysis, recommendations about how to use MBA in blended cement pastes and AAM were provided. The findings of this study are summarized as follows:

- The chemical and mineralogical compositions of MBA are similar to those of the MSWI bottom ash reported in the literature. The amorphous content in MBA is slightly lower than Class F coal fly ash (FA), but much lower than blast furnace slag (BFS). The amorphous phase of MBA has a chemical composition falling within the same range as that of Class F coal fly ash. Calculating the relative contents of SiO_2, CaO, and Al_2O_3 (such as the CaO/SiO_2 and SiO_2/Al_2O_3 ratios) in the amorphous phase can be used as a simplified method to select the AAM precursors that may have high reactivity.
- When using the rapid, relevant, and reliable (R^3) methods to measure the pozzolanic reactivity of MBA, the effect of metallic Al on the test results needs to be considered. The reactivity of MBA as AAM

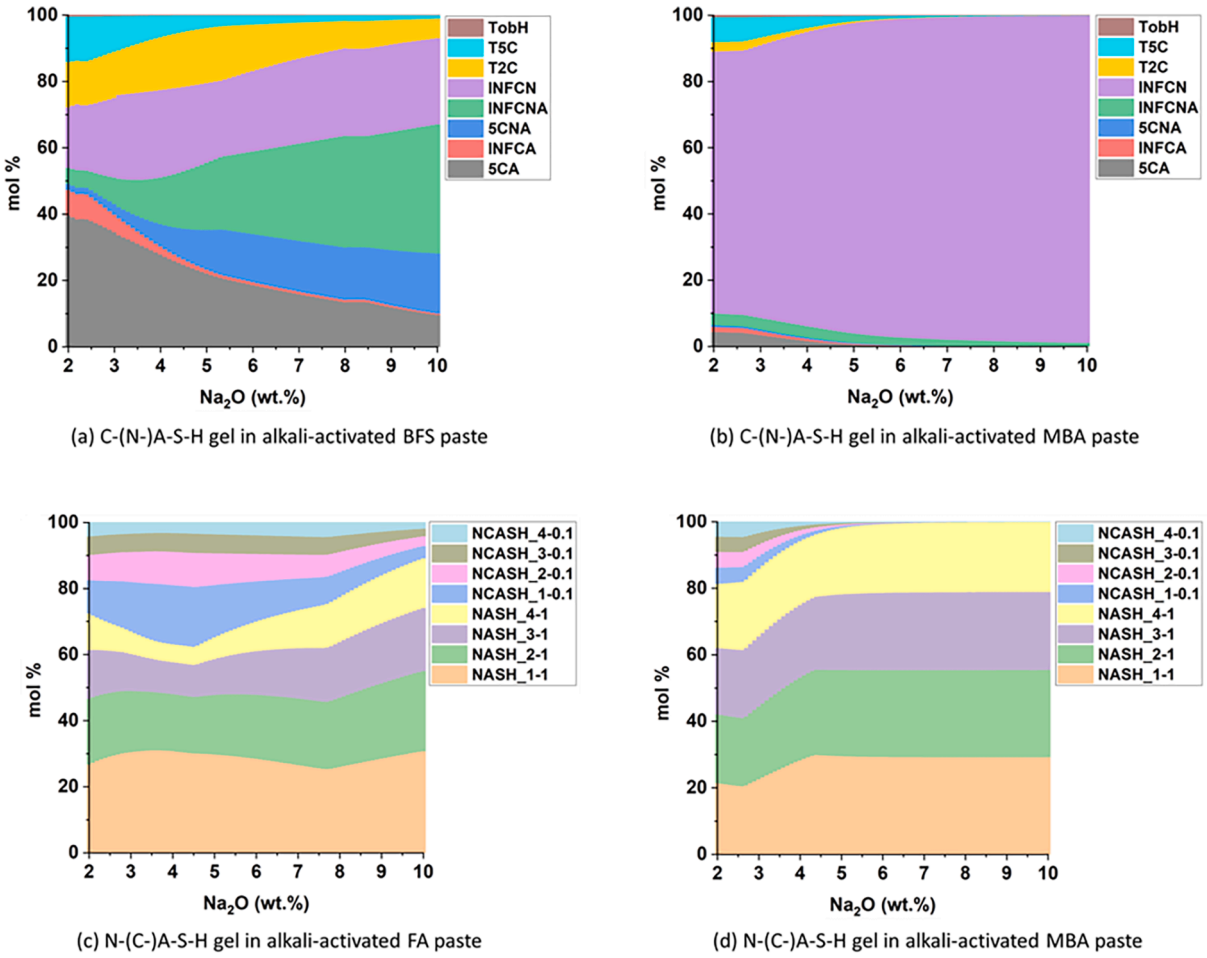

Fig. A1. (a) and (b) Molar percentages of the end-members in the solid solution used for the description of the C-(N-)A-S-H gel predicted in alkali-activated MBA paste and alkali-activated BFS paste. (c) and (d) Molar percentages of the end-members in the solid solution used for the description of the N-(C-)A-S-H gel predicted in alkali-activated MBA paste and alkali-activated FA paste. These end-members were defined in the N(C)ASH_ss model [56] and C(N)ASH_ss model [54]. Detailed information about these end-members can be found in Table 1 and Table 3. The data is presented as a function of the Na2O content in the activator. The percentage of Na2O is with respect to the mass of the precursor.

precursor can be measured by dissolution tests. The dissolution test results provide information about the early-age reaction of MBA. According to the dissolution test of MBA, the molar ratio of dissolved Si/Al is much lower than the optimal value (1.9), indicating that alkali-activated MBA may have low early-age strength. It is recommended to add soluble Si or more reactive Si-enriched precursors into MBA-based AAM to increase the early-age strength.

- Thermodynamic modeling is a promising method to guide the mix design of MBA-based AAM. The chemical and mineralogical compositions of MBA are within the same ranges as the compositions of MSWI bottom ash used by previous researchers. The phase assemblages of alkali-activated MBA paste predicted by thermodynamic modeling are in good agreement with the experimental results reported in the literature. The modeling results for the composition and the pH of the pore solution in alkali-activated MBA provide indications about the reaction of MBA. The predicted pH value can be used to analyze the risk of contaminants leaching from the MBA-based AAM.
- The accuracy of thermodynamic modeling results is determined by the ideal solid solution model used for the simulation of the gel phases. Given that the composition of the amorphous phase in MSWI bottom ash is within the same range as Class F coal fly ash, it is recommended to extend the N(C)ASH_ss model proposed for Class F coal fly ash and improve its accuracy in predicting the reaction products of alkali-activated MSWI bottom ash. The experimental study of the solid phase evolution of alkali-activated MSWI bottom ash pastes is required to validate the simulated solid phase evolution. Considering the wide variety of the MSWI bottom ash produced in the world, it is recommended to study the ones with representative chemical and mineralogical compositions.
- As SCM and AAM precursor, the reactivity of MBA is close to FA but much lower than BFS. When MBA is used to prepare blended cement pastes and alkali-activated pastes, the mix design can refer to previous experience with the pastes prepared with Class F coal fly ash. However, it is necessary to determine the threshold value for the metallic Al content in MBA. The dosage of MBA in blended cement pastes and alkali-activated pastes should not exceed 50 wt% to avoid the excessive leaching of contaminants (especially antimony and sulfates) into the environment.

CRediT authorship contribution statement

Boyu Chen: Conceptualization, Data curation, Formal analysis, Investigation, Methodology, Writing – original draft, Writing – review & editing. **Yibing Zuo:** Methodology, Software, Writing – review & editing. **Shizhe Zhang:** Investigation, Writing – review & editing. **Luiz Miranda de Lima Junior:** . **Xuhui Liang:** Investigation, Writing – review & editing. **Yun Chen:** Investigation, Writing – review & editing. **Marc Brito van Zijl:** . **Guang Ye:** Supervision, Writing – review & editing.

Declaration of Competing Interest

The authors declare that they have no known competing financial interests or personal relationships that could have appeared to influence the work reported in this paper.

Data availability

The authors do not have permission to share data.

Acknowledgments

Boyu Chen would like to thank the Chinese Scholarship Council for their support for her Ph.D. study. Financial support by Mineralz (Part of Renewi) is acknowledged. Special acknowledgment is given to professor Klaas van Breugel for his help with the improvement of text writing. Dr. Nicola Döbelin from RMS Foundation is gratefully acknowledged for the QXRD analysis. Ruud Hendrix at the Department of Materials Science and Engineering of the Delft University of Technology is acknowledged for the X-ray analysis. Arjan Thijssen, Ton Blom, Maiko van Leeuwen, and John van de Berg, from the Stevin lab and Microlab at the Faculty of Civil Engineering and Geosciences, Delft University of Technology, are acknowledged for their support for all the experiments.

Appendix A

Thermodynamic modeling was used to predict the reaction products that could form after the alkali activation of mechanically treated MSWI bottom ash (MBA), Class F coal fly ash(FA), or blast furnace slag (BFS). According to thermodynamic modeling, the gel phases formed in alkali-activated MBA paste will be C-(N-)A-S-H gel and N-(C-)A-S-H gel. The gel phase generated upon the alkali activation of BFS is C-(N-)A-S-H gel. The N-(C-)A-S-H gel is the amorphous reaction product formed in alkali-activated FA paste. The chemical composition of the gel formed in alkali-activated MBA paste is compared with that of the gel formed in alkali-activated BFS paste and alkali-activated FA paste, respectively. Detailed information is presented in the following sections.

- **Predicted C-(N-)A-S-H gel**

In thermodynamic calculation, the chemistry of the C-(N-)A-S-H was simulated by the sublattice solid solution. The changes in the solid solution reflect the structure and composition changes of the C-(N-)A-S-H gel. Figure A 1 (a) and (b) provide information about the end-members chosen within the CNASH_ss model to define the C-(N-)A-S-H gel in alkali-activated BFS paste and alkali-activated MBA paste.

As illustrated in Fig. A1 (a), the solid solution used to describe the chemistry of the C-(N-)A-S-H gel in alkali-activated BFS paste consists of eight end-members. The molar percentages of the C-A-S-H end-members (5CA, INFCA) and the C-S-H end member (T5C) in the solid solution model decreased with increasing Na_2O content in the activator. Meanwhile, the molar percentages of C-N-A-S-H end-members (INFCNA and 5CNA) increased in the solid solution model. The C-N-A-S-H end-members have a higher Na content than the C-A-S-H and C-S-H end-members. This composition change in the solid solution indicates that the Na content of C-(N-)A-S-H gel in alkali-activated BFS paste would increase after increasing the Na_2O content in the activator.

For alkali-activated MBA paste (see Fig. A1 (b)), the C-N-S-H end-member (INFCN) was the dominant component of the solid solution used for the description of the C-(N-)A-S-H gel. The INFCN has a Ca/Si molar ratio of 0.67 (see Table 1). This value is lower than most end-members selected in the solid solution that represents the chemical composition of the C-(N-)A-S-H gel in alkali-activated BFS paste. Accordingly, the Ca/Si molar ratio of the C-(N-)A-S-H gel in alkali-activated MBA paste could be much lower than that in alkali-activated BFS paste. The lower Ca/Si in the C-(N-)A-S-H gel of alkali-activated MBA paste can be attributed to the lower CaO content in the amorphous phase of MBA (Table 8).

Apart from the C-N-S-H end-member (INFCN), the solid solution used to describe the C-(N-)A-S-H gel of alkali-activated MBA paste also includes C-A-S-H end-members (INFCA, 5CA) and C-N-A-S-H end-member (INFCNA). The total amount of these Al-bearing constituents in the solid solution was predicted to be less than 10 mol%, and their molar percentages decreased with the increase in Na_2O content. In the case of alkali-activated BFS paste, much more Al-bearing end-members (54 to 67 mol %) were included in the solid solution to simulate the C-(N-)A-S-H gel. This forecast suggests that the C-(N-)A-S-H gel formed in alkali-activated MBA paste would incorporate much less Al than that in alkali-activated BFS paste. The low Al content in the C-(N-)A-S-H gel of alkali-activated MBA paste could be explained by the low Al_2O_3 content (7.9 wt%) in the amorphous phase of MBA.

In addition, as predicted by the modeling, the total amount of the C-S-H end-members in the solid solution would not exceed 15 mol% for the C-(N-)A-S-H gel of alkali-activated MBA paste. At the same Na_2O wt.%, the molar percentages of the C-S-H end-members in the solid solution representing the C-(N-)A-S-H gel in alkali-activated MBA paste was forecast to be much lower relative to alkali-activated BFS paste (Figure A 1 (a) and (b)). For alkali-activated MBA paste, the molar percentages of the C-S-H end-members in the solid solution decreased with the increase of Na_2O content. The C-S-H end-members (T2C, T5C, TobH) selected in the solid solution model to define the C-(N-)A-S-H gel were derived from the downscaled CSH3Tmodel [61]. The C-S-H end-members defined in the CSH3T model have a Ca/Si ratio between 0.67 and 1.5.

According to Zhu et al. [59], the chemical structure of the C-S-H gel formed in alkali-activated MSWI bottom ash paste was similar to that detected in 10-month Portland cement paste. Although the C-S-H end-members belonging to the CSHQ model were selected in the database, these endmembers were chosen by the model for the simulation of the C-(N-)A-S-H gel in alkali-activated MBA paste. The CSHQ model [33,61] is usually used in the thermodynamic modeling of Portland cement [61]. The Ca/Si ratio of the C-S-H gel described in the CSHQ model ranges from 0.67 to 2.25 [61]. A possible explanation for this prediction could be that the amorphous phase of MBA has much less CaO than cement clinker [168], resulting in a lower Ca/Si ratio of the C-S-H gel. In comparison, the CaO content (determined by XRF) in the MSWI bottom ash used by Zhu et al. [59] was almost two times that in MBA. The C-S-H gel synthesized by Zhu et al. [59] could have a higher Ca/Si ratio and thus was more similar to the C-S-H gel of Portland cement.

- **Predicted N-(C-)A-S-H gel**

The compositions of the solid solution used for the description of the chemistry of the N-(C-)A-S-H gel in alkali-activated FA paste and alkali-activated MBA paste are shown in Figure A 1 (c) and (d). The solid solution representing the N-(C-)A-S-H gel in alkali-activated MBA paste was predicted to mainly consist of the N-A-S-H end-members. The N-A-S-H end-members were also expected to be the main components of the N-(C-)A-S-H gel formed after the alkali activation of FA. These modeling results about the solid solution suggest that the N-(C-)A-S-H gel in alkali-activated MBA paste and alkali-activated FA paste could be similar in chemical structure and composition. This prediction is consistent with the experimental results reported by Zhu et al. [59,60]. In their research, the aluminate silicate gel found in alkali-activated MSWI bottom ash paste had a chemical structure similar to that found in the 180-day alkali-activated Class F coal fly ash.

In addition to the N-A-S-H end-members, the N-C-A-S-H end-members were also included in the solid solution model to consider the uptake of Ca by N-A-S-H gel in alkali-activated MBA paste and alkali-activated FA paste. Compared with alkali-activated FA paste, the proportions of these Ca-bearing end-members selected to model the N-(C-)A-S-H gel in alkali-activated MBA paste were smaller. For alkali-activated MBA paste, the Ca-bearing end-members in the solid

solution decreased from around 20 mol% to zero when increasing the Na_2O content from 2 to 10 wt% in the activator. For alkali-activated FA paste, the total amount of N-C-A-S-H end-members in the solid solution was in the range of 15 to 40 mol %. The prediction about the Ca-bearing end-members indicates that the Ca content of the N-(C-)A-S-H gel in alkali-activated MBA paste would be lower than that in alkali-activated FA paste.

References

[1] S. Kaza, L. Yao, P. Bhada-Tata, F. Van Woerden, What a waste 2.0: a global snapshot of solid waste management to 2050, The World Bank, 2018.
[2] National Bureau of Statistics, (2022). https://data.stats.gov.cn/easyquery.htm?cn=E0103.
[3] I. Renewable Energy Agency, Renewable Capacity Statistics 2022 Statistiques De Capacité Renouvelable 2022 Estadísticas De Capacidad Renovable 2022, (2022). http://www.irena.org.
[4] Municipal waste statistics - Statistics Explained, 2023. https://ec.europa.eu/eurostat/statistics-explained/index.php?title=Municipal_waste_statistics#Municipal_waste_generation.
[5] National Overview: Facts and Figures on Materials, Wastes and Recycling | US EPA, (2022). https://www.epa.gov/facts-and-figures-about-materials-waste-and-recycling/national-overview-facts-and-figures-materials.
[6] A.U. Zaman, Comparative study of municipal solid waste treatment technologies using life cycle assessment method, Int. J. Environ. Sci. Technol. 7 (2010) 225–234, https://doi.org/10.1007/BF03326132.
[7] M. Li, J. Xiang, S. Hu, L. Sun, S. Su, P. Li, X. Sun, Characterization of solid residues from municipal solid waste incinerator, Fuel 83 (2004) 1397–1405.
[8] T. Sabbas, A. Polettini, R. Pomi, T. Astrup, O. Hjelmar, P. Mostbauer, G. Cappai, G. Magel, S. Salhofer, C. Speiser, Management of municipal solid waste incineration residues, Waste Manag 23 (2003) 61–88. https://www.sciencedirect.com/science/article/pii/S0956053X02001617.
[9] Z. Phua, A. Giannis, Z.L. Dong, G. Lisak, W.J. Ng, Characteristics of incineration ash for sustainable treatment and reutilization, Environ. Sci. Pollut. Res. 26 (2019) 16974–16997, https://doi.org/10.1007/s11356-019-05217-8.
[10] J.M. Chimenos, M. Segarra, M.A. Fernandez, F. Espiell, Characterization of the bottom ash in municipal solid waste incinerator, J. Hazard. Mater. A. 64 (1999) 211–222.
[11] K.L. Lin, D.F. Lin, Hydration characteristics of municipal solid waste incinerator bottom ash slag as a pozzolanic material for use in cement, Cem. Concr. Compos. 28 (2006) 817–823, https://doi.org/10.1016/j.cemconcomp.2006.03.003.
[12] R.M. Andrew, Global CO 2 emissions from cement production, Earth Syst. Sci. Data 10 (2018) 195–217.
[13] Cement Industry Energy and CO2 performance "Getting the Numbers Right," (2009). http://docs.wbcsd.org/2009/06/CementIndustryEnergyAndCO2Performance.pdf#:~:text=The WBCSD Cement Sustainability Initiative "Getting the Numbers, industry is monitoring and addressing its emission trends.
[14] B.C. McLellan, R.P. Williams, J. Lay, A. Van Riessen, G.D. Corder, Costs and carbon emissions for geopolymer pastes in comparison to ordinary portland cement, J. Clean. Prod. 19 (2011) 1080–1090.
[15] G. Habert, C. Ouellet-Plamondon, Recent update on the environmental impact of geopolymers, RILEM Tech. Lett. 1 (2016) 17–23.
[16] G. Habert, J.B.D. De Lacaillerie, N. Roussel, An environmental evaluation of geopolymer based concrete production: reviewing current research trends, J. Clean. Prod. 19 (2011) 1229–1238.
[17] G. Habert, A method for allocation according to the economic behaviour in the EU-ETS for by-products used in cement industry, Int. J. Life Cycle Assess. 18 (2013) 113–126.
[18] M. Weil, K. Dombrowski, A. Buchwald, Life-cycle analysis of geopolymers, in: Geopolymers, Elsevier, 2009, pp. 194–210.
[19] T.S. Ng, Y.L. Voo, S.J. Foster, Sustainability with ultra-high performance and geopolymer concrete construction, in: Innov. Mater. Tech. Concr. Constr., Springer, 2012, pp. 81–100.
[20] T. Stengel, D. Heinz, J. Reger, Life cycle assessment of geopolymer concrete–what is the environmental benefit. Proceeding 24th Bienn. Conf. Concr. Inst. Aust., 2009.
[21] P. den Heede, N. De Belie, Environmental impact and life cycle assessment (LCA) of traditional and 'green'concretes: literature review and theoretical calculations, Cem. Concr. Compos. 34 (2012) 431–442.
[22] A. Heath, K. Paine, M. McManus, Minimising the global warming potential of clay based geopolymers, J. Clean. Prod. 78 (2014) 75–83.
[23] J.L. Provis, Alkali-activated materials, Cem. Concr. Res. 114 (2018) 40–48, https://doi.org/10.1016/j.cemconres.2017.02.009.
[24] Cement technology Roadmap 2009 Carbon emission reductions up to 2025, 2018. https://www.wbcsd.org/contentwbc/download/4586/61682/1.
[25] Technology Roadmap Low-Carbon Transition in the Cement Industry, 2018. https://www.wbcsd.org/contentwbc/download/4586/61682/1.
[26] P. Tang, W. Chen, D. Xuan, Y. Zuo, C.S. Poon, Investigation of cementitious properties of different constituents in municipal solid waste incineration bottom ash as supplementary cementitious materials, J. Clean. Prod. 258 (2020), https://doi.org/10.1016/j.jclepro.2020.120675.
[27] W. Zhu, P.J. Teoh, Y. Liu, Z. Chen, E.H. Yang, Strategic utilization of municipal solid waste incineration bottom ash for the synthesis of lightweight aerated alkali-activated materials, J. Clean. Prod. 235 (2019) 603–612, https://doi.org/10.1016/j.jclepro.2019.06.286.
[28] B. Chen, P. Perumal, M. Illikainen, G. Ye, A review on the utilization of municipal solid waste incineration (MSWI) bottom ash as a mineral resource for construction materials, J. Build. Eng. (2023), 106386, https://doi.org/10.1016/j.jobe.2023.106386.
[29] J.L. Provis, S.A. Bernal, Geopolymers and related alkali-activated materials, Annu. Rev. Mat. Res. 44 (2014) 299–327.
[30] P. Duxson, A. Fernández-Jiménez, J.L. Provis, G.C. Lukey, A. Palomo, J.S.J. van Deventer, Geopolymer technology: the current state of the art, J. Mater. Sci. 42 (2007) 2917–2933, https://doi.org/10.1007/s10853-006-0637-z.
[31] I. Lancellotti, C. Ponzoni, L. Barbieri, C. Leonelli, Alkali activation processes for incinerator residues management, Waste Manag. 33 (2013) 1740–1749, https://doi.org/10.1016/j.wasman.2013.04.013.
[32] A. Maldonado-Alameda, J. Giro-Paloma, A. Svobodova-Sedlackova, J. Formosa, J. M. Chimenos, Municipal solid waste incineration bottom ash as alkali-activated cement precursor depending on particle size, J. Clean. Prod. 242 (2020), https://doi.org/10.1016/j.jclepro.2019.118443.
[33] B. Lothenbach, D.A. Kulik, T. Matschei, M. Balonis, L. Baquerizo, B. Dilnesa, G. D. Miron, R.J. Myers, Cemdata18: A chemical thermodynamic database for hydrated Portland cements and alkali-activated materials, Cem. Concr. Res. 115 (2019) 472–506, https://doi.org/10.1016/j.cemconres.2018.04.018.
[34] R.J. Myers, S.A. Bernal, J.L. Provis, Phase diagrams for alkali-activated slag binders, Cem. Concr. Res. 95 (2017) 30–38, https://doi.org/10.1016/j.cemconres.2017.02.006.
[35] R. Xiao, X. Jiang, M. Zhang, P. Polaczyk, B. Huang, Analytical investigation of phase assemblages of alkali-activated materials in CaO-SiO2-Al2O3 systems: The management of reaction products and designing of precursors, Mater. Des. 194 (2020), 108975, https://doi.org/10.1016/j.matdes.2020.108975.
[36] J. Giro-Paloma, A. Maldonado-Alameda, J. Formosa, L. Barbieri, J.M. Chimenos, I. Lancellotti, Geopolymers based on the valorization of Municipal Solid Waste Incineration residues, in: IOP Conf. Ser. Mater. Sci. Eng., Institute of Physics Publishing, 2017. https://doi.org/10.1088/1757-899X/251/1/012125.
[37] A. Keulen, A. Van Zomeren, P. Harpe, W. Aarnink, H.A.E. Simons, H.J. H. Brouwers, High performance of treated and washed MSWI bottom ash granulates as natural aggregate replacement within earth-moist concrete, Waste Manag. 49 (2016) 83–95, https://doi.org/10.1016/j.wasman.2016.01.010.
[38] NEN Connect - NEN-EN 15167-1 (2006). https://connect.nen.nl/Standard/Detail/109308?compId=10037&collectionId=0.
[39] NEN Connect - NEN-EN 1744-1:2009+A1 (2012). https://connect.nen.nl/Standard/Detail/178537?compId=10037&collectionId=0.
[40] N. Doebelin, R. Kleeberg, Profex: a graphical user interface for the Rietveld refinement program BGMN, J. Appl. Cryst. 48 (2015) 1573–1580, https://doi.org/10.1107/S1600576715014685.
[41] B. Chen, M.B. van Zijl, A. Keulen, G. Ye, Thermal treatment on MSWI bottom ash for the utilisation in alkali activated materials, KnE Eng. (2020), https://doi.org/10.18502/keg.v5i4.6792.
[42] Y. Ma, Microstructure and Engineering Properties of Alkali Activated Fly Ash-as an environment friendly alternative to Portland cement, (2013).
[43] S. Zhang, A. Keulen, K. Arbi, G. Ye, Waste glass as partial mineral precursor in alkali-activated slag/fly ash system, Cem. Concr. Res. 102 (2017) 29–40, https://doi.org/10.1016/j.cemconres.2017.08.012.
[44] NEN Connect - NEN-EN 196-2 (2013). https://connect.nen.nl/Standard/Detail/184482?compId=10037&collectionId=0.
[45] B. Chen, Utilization of mswi bottom ash as a mineral resource for low-carbon construction materials: Quality-upgrade treatments, mix design method, and microstructure analysis, (2023).
[46] X. Li, R. Snellings, M. Antoni, N.M. Alderete, M. Ben Haha, S. Bishnoi, Ö. Cizer, M. Cyr, K. De Weerdt, Y. Dhandapani, Reactivity tests for supplementary cementitious materials: RILEM TC 267-TRM phase 1, Mater. Struct. 51 (2018) 1–14.
[47] Standard Test Methods for Measuring the Reactivity of Supplementary Cementitious Materials by Isothermal Calorimetry and Bound Water, Measurements (2020). https://www.astm.org/c1897-20.html.
[48] P. Tang, M.V.A. Florea, P. Spiesz, H.J.H. Brouwers, Application of thermally activated municipal solid waste incineration (MSWI) bottom ash fines as binder substitute, Cem. Concr. Compos. 70 (2016) 194–205, https://doi.org/10.1016/j.cemconcomp.2016.03.015.
[49] R. Snellings, Solution-controlled dissolution of supplementary cementitious material glasses at pH 13: the effect of solution composition on glass dissolution rates, J. Am. Ceram. Soc. 96 (2013) 2467–2475.
[50] A. Schöler, F. Winnefeld, M. Ben Haha, B. Lothenbach, The effect of glass composition on the reactivity of synthetic glasses, J. Am. Ceram. Soc. 100 (2017) 2553–2567.
[51] Y. Zuo, M. Nedeljković, G. Ye, Pore solution composition of alkali-activated slag/fly ash pastes, Cem. Concr. Res. 115 (2019) 230–250.
[52] T. Wagner, D.A. Kulik, F.F. Hingerl, S.V. Dmytrieva, GEM-Selektor geochemical modeling package: TSolMod library and data interface for multicomponent phase models, Can. Mineral. 50 (2012) 1173–1195.
[53] D.A. Kulik, T. Wagner, S.V. Dmytrieva, G. Kosakowski, F.F. Hingerl, K. V. Chudnenko, U.R. Berner, GEM-Selektor geochemical modeling package: revised algorithm and GEMS3K numerical kernel for coupled simulation codes, Comput. Geosci. 17 (2013) 1–24.

[54] R.J. Myers, S.A. Bernal, J.L. Provis, A thermodynamic model for C-(N-)A-S-H gel: CNASH_ss. Derivation and validation, Cem. Concr. Res. 66 (2014) 27–47, https://doi.org/10.1016/j.cemconres.2014.07.005.

[55] R.J. Myers, B. Lothenbach, S.A. Bernal, J.L. Provis, Thermodynamic modelling of alkali-activated slag cements, Appl. Geochem. 61 (2015) 233–247, https://doi.org/10.1016/j.apgeochem.2015.06.006.

[56] Y. Zuo, Experimental Study and Numerical Simulation of the Reaction Process and Microstructure Formation of Alkali-Activated Materials, Delft University of Technology, 2019.

[57] À. Maldonado-Alameda, J. Giro-Paloma, A. Alfocea-Roig, J. Formosa, J. M. Chimenos, Municipal solid waste incineration bottom ash as sole precursor in the alkali-activated binder formulation, Appl. Sci. 10 (2020), https://doi.org/10.3390/APP10124129.

[58] G. Huang, K. Yang, L. Chen, Z. Lu, Y. Sun, X. Zhang, Y. Feng, Y. Ji, Z. Xu, Use of pretreatment to prevent expansion and foaming in high-performance MSWI bottom ash alkali-activated mortars, Constr. Build. Mater. 245 (2020), https://doi.org/10.1016/j.conbuildmat.2020.118471.

[59] W. Zhu, X. Chen, L.J. Struble, E.H. Yang, Characterization of calcium-containing phases in alkali-activated municipal solid waste incineration bottom ash binder through chemical extraction and deconvoluted Fourier transform infrared spectra, J. Clean. Prod. 192 (2018) 782–789, https://doi.org/10.1016/j.jclepro.2018.05.049.

[60] W. Zhu, X. Chen, L.J. Struble, E.H. Yang, Quantitative characterization of aluminosilicate gels in alkali-activated incineration bottom ash through sequential chemical extractions and deconvoluted nuclear magnetic resonance spectra, Cem. Concr. Compos. 99 (2019) 175–180, https://doi.org/10.1016/j.cemconcomp.2019.03.014.

[61] D.A. Kulik, Improving the structural consistency of C-S-H solid solution thermodynamic models, Cem. Concr. Res. 41 (2011) 477–495, https://doi.org/10.1016/j.cemconres.2011.01.012.

[62] NEN Connect - NEN-EN 12457-4 (2002). https://connect.nen.nl/Standard/Detail/82471?compId=10037&collectionId=0.

[63] Soil Quality Decree, 2015. [Online]. Available: http://wetten.overheid.nl/BWBR0023085/BijlageA/geldigheidsdatum_09-10-2015 (2015).

[64] E. Loginova, D.S. Volkov, P.M.F. van de Wouw, M.V.A. Florea, H.J.H. Brouwers, Detailed characterization of particle size fractions of municipal solid waste incineration bottom ash, J. Clean. Prod. 207 (2019) 866–874, https://doi.org/10.1016/j.jclepro.2018.10.022.

[65] U. Müller, K. Rübner, The microstructure of concrete made with municipal waste incinerator bottom ash as an aggregate component, Cem. Concr. Res. 36 (2006) 1434–1443, https://doi.org/10.1016/j.cemconres.2006.03.023.

[66] D. Xuan, C.S. Poon, Removal of metallic Al and Al/Zn alloys in MSWI bottom ash by alkaline treatment, J. Hazard. Mater. 344 (2018) 73–80, https://doi.org/10.1016/j.jhazmat.2017.10.002.

[67] NEN Connect - NEN-EN 206:2014+A2 (2021). https://connect.nen.nl/Standard/Detail/3650677?compId=10037&collectionId=0.

[68] T.P. Seward III, T. Vascott, High temperature glass melt property database for process modeling, Wiley-American Ceramic Society, 2005.

[69] D. Glosser, P. Suraneni, O.B. Isgor, W.J. Weiss, Using glass content to determine the reactivity of fly ash for thermodynamic calculations, Cem. Concr. Compos. 115 (2021), 103849, https://doi.org/10.1016/j.cemconcomp.2020.103849.

[70] Z. Sun, A. Vollpracht, One year geopolymerisation of sodium silicate activated fly ash and metakaolin geopolymers, Cem. Concr. Compos. 95 (2019) 98–110, https://doi.org/10.1016/j.cemconcomp.2018.10.014.

[71] A. Schöler, B. Lothenbach, F. Winnefeld, M. Zajac, Hydration of quaternary Portland cement blends containing blast-furnace slag, siliceous fly ash and limestone powder, Cem. Concr. Compos. 55 (2015) 374–382, https://doi.org/10.1016/j.cemconcomp.2014.10.001.

[72] G.V.P. Bhagath Singh, K.V.L. Subramaniam, Quantitative XRD study of amorphous phase in alkali activated low calcium siliceous fly ash, Constr. Build. Mater. 124 (2016) 139–147, https://doi.org/10.1016/j.conbuildmat.2016.07.081.

[73] C.R. Ward, D. French, Determination of glass content and estimation of glass composition in fly ash using quantitative X-ray diffractometry, Fuel 85 (2006) 2268–2277, https://doi.org/10.1016/j.fuel.2005.12.026.

[74] Y. Jin, W. Feng, D. Zheng, Z. Dong, H. Cui, Structure refinement of fly ash in connection with its reactivity in geopolymerization, Waste Manag. 118 (2020) 350–359, https://doi.org/10.1016/j.wasman.2020.08.049.

[75] G.B. Singh, K.V. Subramaniam, Characterization of Indian fly ashes using different experimental techniques, Indian Concr. J. 92 (2018) 10–23.

[76] B. Valentim, A. Guedes, D. Flores, C.R. Ward, J.C. Hower, Variations in fly ash composition with sampling location: Case study from a Portuguese power plant, (2010).

[77] S. Chithiraputhiran, N. Neithalath, Isothermal reaction kinetics and temperature dependence of alkali activation of slag, fly ash and their blends, Constr. Build. Mater. 45 (2013) 233–242.

[78] J.J. Thomas, A.J. Allen, H.M. Jennings, Density and water content of nanoscale solid C-S–H formed in alkali-activated slag (AAS) paste and implications for chemical shrinkage, Cem. Concr. Res. 42 (2012) 377–383.

[79] K. Gong, C.E. White, Impact of chemical variability of ground granulated blast-furnace slag on the phase formation in alkali-activated slag pastes, Cem. Concr. Res. 89 (2016) 310–319.

[80] H. Ye, A. Radlińska, Quantitative analysis of phase assemblage and chemical shrinkage of alkali-activated slag, J. Adv. Concr. Technol. 14 (2016) 245–260.

[81] N. Marjanović, M. Komljenović, Z. Baščarević, V. Nikolić, R. Petrović, Physical–mechanical and microstructural properties of alkali-activated fly ash–blast furnace slag blends, Ceram. Int. 41 (2015) 1421–1435.

[82] R. Cao, S. Zhang, N. Banthia, Y. Zhang, Z. Zhang, Interpreting the early-age reaction process of alkali-activated slag by using combined embedded ultrasonic measurement, thermal analysis, XRD, FTIR and SEM, Compos. B Eng. 186 (2020), 107840.

[83] Z. Sun, A. Vollpracht, Isothermal calorimetry and in-situ XRD study of the NaOH activated fly ash, metakaolin and slag, Cem. Concr. Res. 103 (2018) 110–122.

[84] F. Puertas, B. González-Fonteboa, I. González-Taboada, M.M. Alonso, M. Torres-Carrasco, G. Rojo, F. Mart'inez-Abella, Alkali-activated slag concrete: Fresh and hardened behaviour, Cem. Concr. Compos. 85 (2018) 22–31.

[85] M. Chi, Effects of dosage of alkali-activated solution and curing conditions on the properties and durability of alkali-activated slag concrete, Constr. Build. Mater. 35 (2012) 240–245.

[86] O. Mikhailova, A. del Campo, P. Rovnanik, J.F. Fernández, M. Torres-Carrasco, In situ characterization of main reaction products in alkali-activated slag materials by Confocal Raman Microscopy, Cem. Concr. Compos. 99 (2019) 32–39.

[87] Y. Zuo, M. Nedeljković, G. Ye, Coupled thermodynamic modelling and experimental study of sodium hydroxide activated slag, Constr. Build. Mater. 188 (2018) 262–279.

[88] S. Puligilla, P. Mondal, Role of slag in microstructural development and hardening of fly ash-slag geopolymer, Cem. Concr. Res. 43 (2013) 70–80.

[89] W. Liu, T. Aldahri, C. Xu, C. Li, S. Rohani, Synthesis of sole gismondine-type zeolite from blast furnace slag during CO2 mineralization process, J. Environ. Chem. Eng. 9 (2021), 104652.

[90] X. Gao, Q.L. Yu, H.J.H. Brouwers, Reaction kinetics, gel character and strength of ambient temperature cured alkali activated slag–fly ash blends, Constr. Build. Mater. 80 (2015) 105–115.

[91] A. Font, L. Soriano, S.M. de Moraes Pinheiro, M.M. Tashima, J. Monzó, M. V. Borrachero, J. Payá, Design and properties of 100% waste-based ternary alkali-activated mortars: Blast furnace slag, olive-stone biomass ash and rice husk ash, J. Clean. Prod. 243 (2020), 118568.

[92] G.M. Kim, J.G. Jang, F. Naeem, H.-K. Lee, Heavy metal leaching, CO 2 uptake and mechanical characteristics of carbonated porous concrete with alkali-activated slag and bottom ash, Int. J. Concr. Struct. Mater. 9 (2015) 283–294.

[93] M. Ben Haha, G. Le Saout, F. Winnefeld, B. Lothenbach, Influence of activator type on hydration kinetics, hydrate assemblage and microstructural development of alkali activated blast-furnace slags, Cem. Concr. Res. 41 (2011) 301–310.

[94] A. Keulen, A. Van Zomeren, J.J. Dijkstra, Leaching of monolithic and granular alkali activated slag-fly ash materials, as a function of the mixture design, Waste Manag. 78 (2018) 497–508.

[95] D. Ravikumar, N. Neithalath, Reaction kinetics in sodium silicate powder and liquid activated slag binders evaluated using isothermal calorimetry, Thermochim Acta 546 (2012) 32–43.

[96] F. Puertas, M. Palacios, H. Manzano, J.S. Dolado, A. Rico, J. Rodríguez, A model for the CASH gel formed in alkali-activated slag cements, J. Eur. Ceram. Soc. 31 (2011) 2043–2056.

[97] S. Ramanathan, M. Croly, P. Suraneni, Comparison of the effects that supplementary cementitious materials replacement levels have on cementitious paste properties, Cem. Concr. Compos. 112 (2020), 103678.

[98] I.G. Lodeiro, N. Cristelo, A. Palomo, A. Fernández-Jiménez, Use of industrial by-products as alkaline cement activators, Constr. Build. Mater. 253 (2020), 119000.

[99] P. Suraneni, J. Weiss, Examining the pozzolanicity of supplementary cementitious materials using isothermal calorimetry and thermogravimetric analysis, Cem. Concr. Compos. 83 (2017) 273–278.

[100] M. Askarian, Z. Tao, B. Samali, G. Adam, R. Shuaibu, Mix composition and characterisation of one-part geopolymers with different activators, Constr. Build. Mater. 225 (2019) 526–537.

[101] J. Aliques-Granero, M.T. Tognonvi, A. Tagnit-Hamou, Durability study of AAMs: Sulfate attack resistance, Constr. Build. Mater. 229 (2019), 117100.

[102] M. Kamath, S. Prashant, M. Kumar, Micro-characterisation of alkali activated paste with fly ash-GGBS-metakaolin binder system with ambient setting characteristics, Constr. Build. Mater. 277 (2021), 122323.

[103] S. Park, H.N. Yoon, J. Seo, H.-K. Lee, J.G. Jang, Structural evolution of binder gel in alkali-activated cements exposed to electrically accelerated leaching conditions, J. Hazard. Mater. 387 (2020), 121825.

[104] Y.J. Zhang, L. Kang, L.C. Liu, Alkali-activated cements for photocatalytic degradation of organic dyes, in: Handb. Alkali-Activated Cem. Mortars Concr., Elsevier, 2015: pp. 729–775.

[105] J. Wang, T. Huang, L. Han, F. Xie, Z. Liu, D. Wang, Optimization of alkali-activated concrete based on the characteristics of binder systems, Constr. Build. Mater. 300 (2021), 123952.

[106] Y. Wang, R. Chen, J. Hu, Z. Zhang, H. Huang, Y. Ma, J. Wei, Z. Zhang, S. Yin, H. Wang, others, Surface characteristics and electrochemical behaviors of passive reinforcing steel in alkali-activated slag, Corros. Sci. 190 (2021), 109657.

[107] A. Nics, N.A. Eren, A. Çevik, Effects of nanosilica and steel fibers on the impact resistance of slag based self-compacting alkali-activated concrete, Ceram. Int. (2021).

[108] O.M. Abdulkareem, A. Ben Fraj, M. Bouasker, L. Khouchaf, A. Khelidj, Microstructural investigation of slag-blended UHPC: The effects of slag content and chemical/thermal activation, Constr. Build. Mater. 292 (2021), 123455.

[109] N.T.A. Júnior, V.M.E. Lima, S.M. Torres, P.E.A. Basto, A.A.M. Neto, Experimental investigation of mix design for high-strength alkali-activated slag concrete, Constr. Build. Mater. 291 (2021), 123387.

[110] Y. Tian, C. Yang, S. Yuan, H. Yuan, K. Yang, L. Yu, M. Zhang, X. Zhu, Understanding the rheological properties of alkali-activated slag pastes from the cohesion and friction interactions, Constr. Build. Mater. 291 (2021), 123311.
[111] M. Teymouri, K. Behfarnia, A. Shabani, Mix design effects on the durability of alkali-activated slag concrete in a hydrochloric acid environment, Sustainability. 13 (2021) 8096.
[112] R. Cai, H. Ye, Clinkerless ultra-high strength concrete based on alkali-activated slag at high temperatures, Cem. Concr. Res. 145 (2021), 106465.
[113] S. Marathe, I.R. Mithanthaya, R.Y. Shenoy, Durability and microstructure studies on Slag-Fly Ash-Glass powder based alkali activated pavement quality concrete mixes, Constr. Build. Mater. 287 (2021), 123047.
[114] F. Moodi, S. Norouzi, P. Dashti, Mechanical properties and durability of alkali-activated slag repair mortars containing silica fume against freeze-thaw cycles and salt scaling attack, Adv. Concr. Constr. 11 (2021) 493–505.
[115] H. Geng, Q. Xu, S.B. Duraman, Q. Li, Effect of rheology of fresh paste on the pore structure and properties of pervious concrete based on the high fluidity alkali-activated slag, Crystals 11 (2021) 593.
[116] G. Fang, Q. Wang, M. Zhang, Micromechanical analysis of interfacial transition zone in alkali-activated fly ash-slag concrete, Cem. Concr. Compos. 119 (2021), 103990.
[117] K. Kondepudi, K.V.L. Subramaniam, Formulation of alkali-activated fly ash-slag binders for 3D concrete printing, Cem. Concr. Compos. 119 (2021), 103983.
[118] L. Mengasini, M. Mavroulidou, M.J. Gunn, Alkali-activated concrete mixes with ground granulated blast furnace slag and paper sludge ash in seawater environments, Sustain. Chem. Pharm. 20 (2021), 100380.
[119] J. Huang, C. Zou, D. Sun, B. Yang, J. Yan, Effect of recycled fine aggregates on alkali-activated slag concrete properties, Structures (2021) 89–99.
[120] A. Alzaza, K. Ohenoja, M. Illikainen, One-part alkali-activated blast furnace slag for sustainable construction at subzero temperatures, Constr. Build. Mater. 276 (2021), 122026.
[121] Z. Li, T. Lu, Y. Chen, B. Wu, G. Ye, Prediction of the autogenous shrinkage and microcracking of alkali-activated slag and fly ash concrete, Cem. Concr. Compos. 117 (2021), 103913.
[122] J. Lei, W.W. Law, E.-H. Yang, Effect of calcium hydroxide on the alkali-silica reaction of alkali-activated slag mortars activated by sodium hydroxide, Constr. Build. Mater. 272 (2021), 121868.
[123] Y. Du, J. Wang, C. Shi, H.-J. Hwang, N. Li, Flexural behavior of alkali-activated slag-based concrete beams, Eng. Struct. 229 (2021), 111644.
[124] S. Uppalapati, L. Vandewalle, Ö. Cizer, Monitoring the setting process of alkali-activated slag-fly ash cements with ultrasonic P-wave velocity, Constr. Build. Mater. 271 (2021), 121592.
[125] S. Rajaei, P. Shoaei, M. Shariati, F. Ameri, H.R. Musaeei, B. Behforouz, J. de Brito, Rubberized alkali-activated slag mortar reinforced with polypropylene fibres for application in lightweight thermal insulating materials, Constr. Build. Mater. 270 (2021), 121430.
[126] G.F. Huseien, A.R.M. Sam, R. Alyousef, Texture, morphology and strength performance of self-compacting alkali-activated concrete: Role of fly ash as GBFS replacement, Constr. Build. Mater. 270 (2021), 121368.
[127] B.H. Tekle, K. Holschemacher, P. Löber, B. Heiden, Mechanical behavior and frost-resistance of alkali-activated cement concrete with blended binder at ambient curing condition, Buildings 11 (2021) 52.
[128] X. Wei, D. Li, F. Ming, C. Yang, L. Chen, Y. Liu, Influence of low-temperature curing on the mechanical strength, hydration process, and microstructure of alkali-activated fly ash and ground granulated blast furnace slag mortar, Constr. Build. Mater. 269 (2021), 121811.
[129] A.M. Humad, J.L. Provis, K. Habermehl-Cwirzen, M. Rajczakowska, A. Cwirzen, Creep and long-term properties of alkali-activated swedish-slag concrete, J. Mater. Civ. Eng. 33 (2021) 4020475.
[130] X. Zhou, Y. Zeng, P. Chen, Z. Jiao, W. Zheng, Mechanical properties of basalt and polypropylene fibre-reinforced alkali-activated slag concrete, Constr. Build. Mater. 269 (2021), 121284.
[131] M.N.N. Khan, A.K. Saha, P.K. Sarker, Evaluation of the ASR of waste glass fine aggregate in alkali activated concrete by concrete prism tests, Constr. Build. Mater. 266 (2021), 121121.
[132] F. Puertas, Escorias de alto horno: composición y comportamiento hidráulico, Mater. Construcción. 43 (1993) 37–48.
[133] I. Garcia-Lodeiro, A. Palomo, A. Fernández-Jiménez, 3 - Crucial insights on the mix design of alkali-activated cement-based binders, in: F. Pacheco-Torgal, J.A. Labrincha, C. Leonelli, A. Palomo, P.B.T.-H. of A.-A.C. Chindaprasirt Mortars and Concretes (Eds.), Woodhead Publishing, Oxford, 2015: pp. 49–73. https://doi.org/https://doi.org/10.1533/9781782422884.1.49.
[134] S. Kucharczyk, M. Sitarz, M. Zajac, J. Deja, The effect of CaO/SiO 2 molar ratio of CaO-Al 2 O 3 -SiO 2 glasses on their structure and reactivity in alkali activated system, Spectrochim Acta Part A Mol. Biomol. Spectrosc. 194 (2018) 163–171, https://doi.org/10.1016/j.saa.2018.01.018.
[135] P. Durdziński, R. Snellings, C.F. Dunant, M. Ben Haha, K.L. Scrivener, Fly ash as an assemblage of model Ca–Mg–Na-aluminosilicate glasses, Cem. Concr. Res. 78 (2015) 263–272.
[136] I. Garcia-Lodeiro, E. Aparicio-Rebollo, A. Fernández-Jimenez, A. Palomo, Effect of calcium on the alkaline activation of aluminosilicate glass, Ceram. Int. 42 (2016) 7697–7707, https://doi.org/10.1016/j.ceramint.2016.01.184.
[137] I. Garcia-Lodeiro, A. Fernández-Jimenez, P. Pena, A. Palomo, Alkaline activation of synthetic aluminosilicate glass, Ceram. Int. 40 (2014) 5547–5558, https://doi.org/10.1016/j.ceramint.2013.10.146.
[138] F. Pacheco-Torgal, J. Castro-Gomes, S. Jalali, Alkali-activated binders: A review. Part 2. About materials and binders manufacture, Constr. Build. Mater. 22 (2008) 1315–1322.
[139] R.A. Fletcher, K.J.D. MacKenzie, C.L. Nicholson, S. Shimada, The composition range of aluminosilicate geopolymers, J. Eur. Ceram. Soc. 25 (2005) 1471–1477.
[140] A. Fernández-Jiménez, A. Palomo, Characterisation of fly ashes. Potential reactivity as alkaline cements☆, Fuel 82 (2003) 2259–2265.
[141] H. Wang, H. Li, F. Yan, Synthesis and mechanical properties of metakaolinite-based geopolymer, Colloids Surfaces A Physicochem. Eng. Asp. 268 (2005) 1–6.
[142] C. Ruiz Santa Quiteria Gómez, Materias primas alternativas para el desarrollo de nuevos cementos: activación alcalina de vidrios silicoaluminosos, (2013).
[143] P. Duxson, S.W. Mallicoat, G.C. Lukey, W.M. Kriven, J.S.J. van Deventer, The effect of alkali and Si/Al ratio on the development of mechanical properties of metakaolin-based geopolymers, Colloids Surfaces A Physicochem. Eng. Asp. 292 (2007) 8–20, https://doi.org/10.1016/j.colsurfa.2006.05.044.
[144] A. Mary Joseph, R. Snellings, P. Nielsen, S. Matthys, N. De Belie, A.M. Joseph, R. Snellings, P. Nielsen, S. Matthys, N. De Belie, Pre-treatment and utilisation of municipal solid waste incineration bottom ashes towards a circular economy, Constr. Build. Mater. 260 (2020), 120485, https://doi.org/10.1016/j.conbuildmat.2020.120485.
[145] J. Petrovic, G. Thomas, Reaction of Aluminum with Water to Produce Hydrogen-2010 Update, 2011.
[146] K.C. Newlands, M. Foss, T. Matchei, J. Skibsted, D.E. Macphee, Early stage dissolution characteristics of aluminosilicate glasses with blast furnace slag-and fly-ash-like compositions, J. Am. Ceram. Soc. 100 (2017) 1941–1955.
[147] Song, H.M. Jennings, Pore solution chemistry of alkali-activated ground granulated blast-furnace slag11This paper was originally submitted to Advanced Cement Based Materials. The paper was received at the Editorial Office of Cement and Concrete Research on 12 November 1998 an, Cem. Concr. Res. 29 (1999) 159–170. https://doi.org/https://doi.org/10.1016/S0008-8846(98)00212-9.
[148] P. Duxson, J.L. Provis, G.C. Lukey, S.W. Mallicoat, W.M. Kriven, J.S.J. van Deventer, Understanding the relationship between geopolymer composition, microstructure and mechanical properties, Colloids Surfaces A Physicochem. Eng. Asp. 269 (2005) 47–58, https://doi.org/10.1016/j.colsurfa.2005.06.060.
[149] J.L. Provis, J.S.J. Van Deventer, Alkali activated materials, Springer Science & Business Media, 2013 state-of-the-art report, RILEM TC 224-AAM,.
[150] W. Zhu, X. Chen, A. Zhao, L.J. Struble, E.H. Yang, Synthesis of high strength binders from alkali activation of glass materials from municipal solid waste incineration bottom ash, J. Clean. Prod. 212 (2019) 261–269, https://doi.org/10.1016/j.jclepro.2018.11.295.
[151] X. Dou, F. Ren, M.Q. Nguyen, A. Ahamed, K. Yin, W.P. Chan, V.W.C. Chang, Review of MSWI bottom ash utilization from perspectives of collective characterization, treatment and existing application, Renew. Sustain. Energy Rev. 79 (2017) 24–38, https://doi.org/10.1016/j.rser.2017.05.044.
[152] V.O. Ozçelik, C.E. White, Nanoscale charge-balancing mechanism in alkali-substituted calcium–silicate–hydrate gels, J. Phys. Chem. Lett. 7 (2016) 5266–5272.
[153] M. Criado, A. Fernández-Jiménez, A.G. De La Torre, M.A.G. Aranda, A. Palomo, An XRD study of the effect of the SiO2/Na2O ratio on the alkali activation of fly ash, Cem. Concr. Res. 37 (2007) 671–679.
[154] Q. Alam, M.V.A. Florea, K. Schollbach, H.J.H. Brouwers, A two-stage treatment for Municipal Solid Waste Incineration (MSWI) bottom ash to remove agglomerated fine particles and leachable contaminants, Waste Manag. 67 (2017) 181–192, https://doi.org/10.1016/j.wasman.2017.05.029.
[155] M. Tella, G.S. Pokrovski, Antimony (III) complexing with O-bearing organic ligands in aqueous solution: An X-ray absorption fine structure spectroscopy and solubility study, Geochim. Cosmochim. Acta 73 (2009) 268–290.
[156] M. Tella, G.S. Pokrovski, Stability and structure of pentavalent antimony complexes with aqueous organic ligands, Chem. Geol. 292 (2012) 57–68.
[157] M. Tella, G.S. Pokrovski, Antimony (V) complexing with O-bearing organic ligands in aqueous solution: an X-ray absorption fine structure spectroscopy and potentiometric study, Mineral. Mag. 72 (2008) 205–209.
[158] S. Steely, D. Amarasiriwardena, B. Xing, An investigation of inorganic antimony species and antimony associated with soil humic acid molar mass fractions in contaminated soils, Environ. Pollut. 148 (2007) 590–598.
[159] G. Ceriotti, D. Amarasiriwardena, A study of antimony complexed to soil-derived humic acids and inorganic antimony species along a Massachusetts highway, Microchem. J. 91 (2009) 85–93.
[160] B. Verbinnen, J. Van Caneghem, P. Billen, C. Vandecasteele, Long term leaching behavior of antimony from MSWI bottom ash: influence of mineral additives and of organic acids, Waste Biomass Valoriz. 8 (2017) 2545–2552, https://doi.org/10.1007/s12649-016-9796-6.
[161] K. Andersson, B. Allard, M. Bengtsson, B. Magnusson, Chemical composition of cement pore solutions, Cem. Concr. Res. 19 (1989) 327–332, https://doi.org/10.1016/0008-8846(89)90022-7.
[162] G. Cornelis, T. Van Gerven, R. Snellings, B. Verbinnen, J. Elsen, C. Vandecasteele, Stability of pyrochlores in alkaline matrices: Solubility of calcium antimonate, Appl. Geochemistry. 26 (2011) 809–817, https://doi.org/10.1016/j.apgeochem.2011.02.002.
[163] X.G. Li, Y. Lv, B.G. Ma, Q. Bin Chen, X.B. Yin, S.W. Jian, Utilization of municipal solid waste incineration bottom ash in blended cement, J. Clean. Prod. 32 (2012) 96–100, https://doi.org/10.1016/j.jclepro.2012.03.038.
[164] B. Guo, B. Liu, J. Yang, S. Zhang, The mechanisms of heavy metal immobilization by cementitious material treatments and thermal treatments: A review, J. Environ. Manage. 193 (2017) 410–422, https://doi.org/10.1016/j.jenvman.2017.02.026.

[165] M. Irannajad, H. Kamran Haghighi, Removal of heavy metals from polluted solutions by zeolitic adsorbents: a review, Environ. Process. 8 (2021) 7–35, https://doi.org/10.1007/s40710-020-00476-x.
[166] J. Zhang, J.L. Provis, D. Feng, J.S.J. van Deventer, Geopolymers for immobilization of Cr6+, Cd2+, and Pb2+, J. Hazard. Mater. 157 (2008) 587–598, https://doi.org/10.1016/j.jhazmat.2008.01.053.
[167] J. Deja, Immobilization of Cr6+, Cd2+, Zn2+ and Pb2+ in alkali-activated slag binders, Cem. Concr. Res. 32 (2002) 1971–1979, https://doi.org/10.1016/S0008-8846(02)00904-3.
[168] P. Hewlett, M. Liska, Lea's chemistry of cement and concrete, Butterworth-Heinemann, 2019.